Entropy Generation for a Bypass Transitional Boundary Layer and Improved Particle Image Velocimetry Measurements Using the Particle Density Information

A Dissertation

Presented in Partial Fulfillment of the Requirements for the

Degree of Doctor of Philosophy

with a

Major in Mechanical Engineering

in the

College of Graduate Studies

University of Idaho

by

Richard S. Skifton

August 2015

Major Professor: Ralph S. Budwig, Ph.D.

Committee Members: John Crepeau, Ph.D.; Tao Xing, Ph.D.; Barton Smith, Ph.D.

Department Administrator: Steven Beyerlein, Ph.D.

Authorization to Submit Dissertation

This dissertation of Richard Skifton, submitted for the degree of Doctor of Philosophy with a Major in Mechanical Engineering and titled "Entropy Generation for a Bypass Transitional Boundary Layer and Improved Particle Image Velocimetry Measurements Using the Particle Density Information," has been reviewed in final form. Permission, as indicated by the signatures and dates given below, is now granted to submit final copies to the College of Graduate Studies for approval.

Major Professor: _____Date:_____
Ralph Budwig, Ph.D.

Committee Members: _____Date:_____
John Crepeau, Ph.D.

_____Date:_____
Tao Xing, Ph.D.

_____Date:_____
Barton Smith, Ph.D.

Department Administrator: _____Date:_____
Steven Beyerlein, Ph.D.

Abstract

The principal purpose of this study is to better understand the pointwise entropy generation rate in bypass, transitional, boundary-layer flow. The experimental work herein, utilized particle image velocimetry (PIV) to measure flow along a flat plate. The flow past the flat plate was under the influence of a "negligible" zero pressure gradient; followed by the installation of an adverse pressure gradient. Further, the boundary layer flow was artificially tripped to turbulence (called "bypass" transition) by means of elevated freestream turbulence. The pointwise entropy generation rate was seen to behave similar to that of published CFD and DNS results. The observations from this work show the decrease of viscous contributions to entropy generation rate through the transition process; while the turbulent contributions of entropy generation rate greatly increase through the same transitional flow. A basic understanding of pointwise entropy generation rate over a flat plate is that a large majority of the contributions come within a $y^+ < 30$. However, a trade off between viscous and turbulent dissipation begins very early on in the flow where a significant amount of the total pointwise entropy generation rate is seen up to the wake region of the boundary layer.

An improvement to the measurement technique of PIV was found when taking measurements very near a wall interface. The particles utilized in PIV form a biased dispersion near interfaces that, in turn, lead to biased velocity measurements. This lack of seeding in the high shear region of the flow *always* biases the velocity measurement high as the particles are, on average, towards the far end of an interrogation window (IW) – opposite of the wall. By observing the ensemble-averaged IW particle-dispersion centroid as the corrected measurement location against the conventional standard of the geometric center of the IW, this paper puts forth a methodology to correct for the biased error in flow measurements very near the wall. A typical correction to the reported velocity measurement *location* within a wall layer flow was

seen to be approximately 75% from the geometric center to the edge of an IW – a significant improvement at relatively low velocities.

Acknowledgements

I would like to thank my advisor, Dr. Ralph Budwig, for showing the type of patience I needed while learning more about fluid dynamics. My committee members, Drs. John Crepeau, Tao Xing, and Barton Smith, were also a significant part of my education, and I am greatly appreciative of their expertise. Lastly, I would like to thank Dr. Donald McEligot for our many conversations over the last 4 years.

I would also like to thank the Department of Energy by means of their Experimental Program to Stimulate Competitive Research (EPSCoR) and Nuclear Energy University Program (NEUP) offices for providing me the type of monetary support I needed to get through this degree.

Dedication

I would like to dedicate this work to my wife, Ashley Skifton. Over the past 8 years she has lived the student life while increasing our family by 4, and has supported me throughout.

Table of Contents

List of Tables

List of Figures

List of Abbreviations

APG	Adverse Pressure Gradient
CFD	Computational Fluid Dynamics
DNS	Direct Numerical Simulation
INL	Idaho National Laboratory
IW	Interrogation Window
LFOV	Large Field of View
LDV	Laser Doppler Velocimetry
MIR	Matched Index of Refraction flow facility
MFOV	Mezzo Field of View
NaN	Not a Number
ODE	Ordinary Differential Equation
PIV	Particle Image Velocimetry
PTV	Particle Tracking Velocimetry
RANS	Reynods-Averaged Navier-Stokes equations
RMS	Root Mean Square
TG	Turbulence Generator
ZPG	Zero Pressure Gradient

Nomenclature

$(\_)_\infty$	freestream conditions
$(\_)^+$	units in wall coordinates
$(\_)''$	per unit surface area
$(\_)'''$	per unit volume
$\overline{(\_)}$, $< \_ >$	time averaged quantity
{ }	function of
#px	actual number of pixels found on camera sensor in x-direction
C_d	dissipation coefficient
C_f	skin friction coefficient, local, $\frac{\tau_w(x)}{\frac{1}{2}\rho U_\infty(x)^2}$
Δpx	desired maximum pixel displacement
δ^*	displacement thickness of the boundary layer
δ or δ_{99}	boundary layer thickness
$\frac{\delta U}{\delta x}$, $\frac{\delta U}{\delta y}$	time averaged streamwise velocity gradient
$\frac{\delta V}{\delta x}$, $\frac{\delta V}{\delta x}$	time averaged normal velocity gradient
$\frac{\delta u}{\delta x}$, $\frac{\delta u}{\delta y}$, $\frac{\delta u}{\delta z}$	instantaneous velocity gradient in streamwise direction
$\frac{\delta v}{\delta x}$, $\frac{\delta v}{\delta y}$, $\frac{\delta v}{\delta z}$	instantaneous velocity gradient in normal direction
$\frac{\delta w}{\delta x}$, $\frac{\delta w}{\delta y}$, $\frac{\delta w}{\delta z}$	instantaneous velocity gradient in spanwise direction
ϵ	indirect or turbulent dissipation rate
η	non-dimenstional Blasius parameter, Kolomogorov length scale
FOV_x	physical dimension of the image in x
$FSTI_x$	free stream turbulent intensity from the x-component of the flow
g	acceleration of gravity
H	shape factor, δ/θ

K_t	acceleration parameter
L	integral length scale
λ	molecular diffusivity
M	turbulence generator rod pitch diameter
μ	fluid dynamic viscosity
ν	kinematic viscosity
p	pressure and pressure fluctuations
Φ	direct or viscous dissipation rate
q^2	sum of the squared velocity fluctuations, $u^2 + v^2 + w^2$
R	Pearson correlation coefficient
ReSS	Reynolds shear stress, units of shear
Re_x	Reynolds number based on distance from leading edge
Re_θ	Reynolds number based on momentum thickness
ρ	fluid density
S‴	entropy generation per unit volume
θ	momentum thickness
T	absolute temperature
t	time
$TI_x(y)$	turbulence intensity from streamwise component, u, measurements in the wall normal direction
$TI_y(y)$	turbulence intensity from normal component, v, measurements in the wall normal direction
Tu	total freestream turbulence intensity, $\sqrt{\frac{1}{3}(\overline{u'^2} + \overline{v'^2} + \overline{w'^2})}/U_\infty$
$\overline{vv}$	time averaged Reynolds normal stress, units of velocity squared
$\overline{uv}$	time averaged Reynolds shear stress, units of velocity squared

U, V, W	time averaged velocity in x, y, and z, respectively
u, v, w	instantaneous, fluctuating component of the velocity in x, y, and z, respectively
U_∞	local streamwise freestream velocity
U_{max}	maximum observable velocity within an image
$U_{RMS}(x)$	root-mean-squared of streamwise velocity fluctuations, $\sqrt{\overline{u'^2}}$
x, y, z	spatial position/coordinates from center of leading edge

Chapter 1

Introduction and Background

The main objective of this dissertation is to obtain understanding of pointwise entropy generation rate in a specific characteristic of wall shear flows, that is "bypass" transitional flow between laminar and turbulent boundary layers. A significant understanding of entropy generation rate from flows of this kind are the principle factors in saving energy and sustainability [20, 45]. This will in turn provide a reduction in fuel consumption, green house gases, and/or waste. The local entropy generation rate per unit volume, S''', ascertains the localized contribution to losses. This study will give a broader understanding of the governing sources of these loses which will help improve the efficiency and sustainability of energy in industry. Entropy generation, S‴, has been the subject of many past studies for laminar and turbulent flows [3], the questions now turn to the transitional stage of fluid flow – specifically that of bypass transition. Bypass transition occurs when the free stream turbulence activates the boundary layer forming on the plate, thus "bypassing" the Tollmein-Schlichting waves [49]. Figure 1.1 is a representation of the "bypass" transition process illustrated by Schlatter *et al.* [47] from a Direct Numerical Simulation (DNS) they performed in a related study.

This scientific research will help improve the understanding of entropy generation in thermal fluid flow above and beyond the current understanding. This will be immensely beneficial, due to its wide range of applicability in turbomachinary, aerodynamics, and other general fluid flow disciplines.

The concept of entropy, S, and its generation are reviewed in Reynolds [43], Bejan [3], and Gilmore [15] among others. Entropy in simple terms is the measurement of chaos or the unavailability of heat to perform work in a cycle, i.e., losses. Entropy generation is a factor in all turbomachinary, and is manifested whenever there is heat

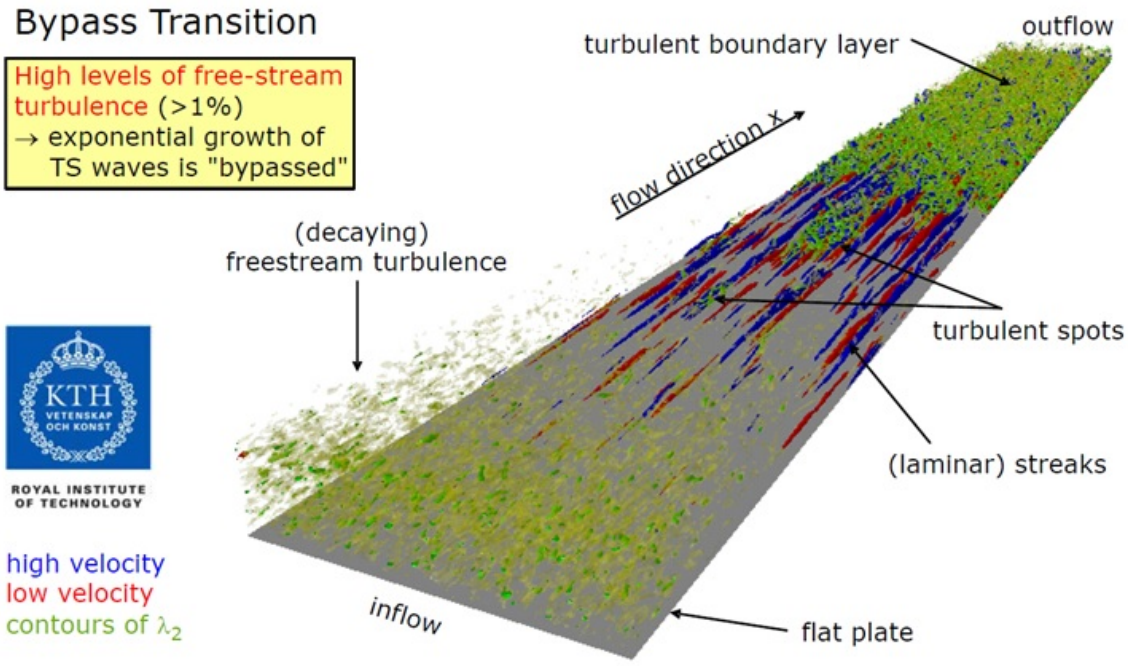

Figure 1.1: DNS model of so-called "bypass" transition [47].

being lost to the surroundings and not being used as a reliable work source.

This research is part of the US Department of Energy effort to advance the energy security of the United States with scientific ingenuity. Likewise, it will assist the Idaho National Laboratory's (INL) mission of providing safe, competitive,and sustainable energy systems.

Chapter 2

Literature Review

For just short of a century, extensive research has been done on the laminar, transitional, and turbulent boundary layers, and on the effects of pressure gradients and free stream turbulence intensities (Schlichting [49], Bradshaw [5], Narasimha [38], Sudar et. al. [52], Mayle [32], Ames and Plesniak [2], Wang et. al. [65], Jacobs and Durbin [21], Matsubara and Alfredsson [31], Volino et. al. [57], Brandt et. al. [6], Schlatter et. al. [47]), but few have actually looked into the entropy being generated. Further, few experiments have had sufficient measurements to calculate the entropy generation. Some at the University of Limerick have previously predicted and measured the local entropy generation rate within transitional boundary layers with streamwise pressure gradients (Walsh et. al. [59] and Griffin *et al.* [16]).

For wall bounded fluid flow, Bejan [3] and Rotta [46] have both shown that most of the entropy generation takes place just beyond the overlap layer ($y^+ < 30$) of the flow adjacent to the wall. Further, they find a significant increase in viscous dissipation at the region so-called "onset of the transition" and beyond. In order to determine S''' within this thin sublayer it is important to obtain instantaneous quantities as ∂v/∂y, ∂w/∂z, etc., and the time-average quantity as the Reynolds shear stress ($-\rho\overline{uv}$). With the largest normal-to-the-wall distance being on the order of 0.1 mm at times, the sublayer can be difficult to measure, as the smallest multi-sensor hot wire anemometer are no smaller than a millimeter (Vukoslavcevic and Wallace [58]). Both the large size and matched index of refraction in the present experiment allow for high fidelity measurements very near the wall (more details will be expressed in Section 3.1)

Bejan [3], among others, have stated the entropy generation rate per unit volume, S$'''$, to be found from the viscous dissipation function Φ for the flow,

$$S'''\{y\} = \frac{\mu\Phi}{T} = \mu\frac{\left[\frac{\delta U}{\delta y} + \frac{\delta V}{\delta x}\right]^2 + 2\left[\frac{\delta U}{\delta x}^2 + \frac{\delta V}{\delta y}^2\right]}{T} \tag{2.1}$$

where it's important to note that the uppercase velocities, U and V, are time averaged velocity measurements; therefore representing the mean/viscous contribution of the flow to entropy generation.

Later, Kock and Herwig [28] added to the viscous dissipation what they called turbulent dissipation, $\rho\epsilon$, which basically takes into account the turbulent kinetic energy being dissipated into thermal energy by

$$\begin{aligned}\rho\epsilon =& 2\mu\left[\overline{\left(\frac{\delta u}{\delta x}\right)^2} + \overline{\left(\frac{\delta v}{\delta y}\right)^2} + \overline{\left(\frac{\delta w}{\delta z}\right)^2}\right] \\ &+ \mu\left[\overline{\left(\frac{\delta u}{\delta y} + \frac{\delta v}{\delta x}\right)^2} + \overline{\left(\frac{\delta v}{\delta z} + \frac{\delta w}{\delta y}\right)^2} + \overline{\left(\frac{\delta w}{\delta x} + \frac{\delta u}{\delta z}\right)^2}\right].\end{aligned} \tag{2.2}$$

Here the velocity measurements are all lower case (e.g. u, v, and w), meaning these are instantaneous gradients that have been squared, and only then time averaged. In other words, the total instantaneous velocity measurement can be written as U+u, which is the mean (capital letter) plus the fluctuating component (lower case letter). Also, this requires instantaneous velocity gradients in *all three* directions. Equation 2.1 and 2.2 together give the complete pointwise entropy generation rate contributions from both viscous and turbulent effects (or direct and indirect, respectively)

$$S''' = \frac{\mu\phi + \rho\epsilon}{T} \tag{2.3}$$

Another, simpler way of looking at entropy generation is with Rotta's [49] approximate approach.

$$S''' \backsimeq \frac{\left[\mu\left(\frac{\delta U}{\delta y}\right)^2 - \rho\overline{uv}\left(\frac{\delta U}{\delta y}\right)\right]}{T} \tag{2.4}$$

which should be noted as only being accurate within a turbulent flow, and away from the wall. Which, unfortunately, has little to no application in the present study.

A look at Walsh *et al.* [63] shows a derivation of entropy generation in integral form by integrating S''' in wall coordinates, and yielding per unit area entropy generation

$$\begin{aligned}\int_0^\delta S'''\{y\}^+dy^+ = S''\{\delta\}^+ \approx &\int_0^\delta (\partial U^+/\partial y^+)^2 dy^+ - \int_0^\delta (\overline{uv})^+(\partial U^+/\partial y^+)dy^+ \\ &- \int_0^\delta \left[\overline{(u^2)^+} - \overline{(v^2)^+}\right](\partial U^+/\partial x^+)dy^+ \\ &- (d/dx^+)\int_0^\delta U^+(1/2)\overline{(q^2)^+}dy^+ \\ &- (1/2)\overline{v_\delta^+\left[(u_\delta^2)^+ + (v_\delta^2)^+ + (w_\delta^2)^+\right]} - \overline{v_\delta^+ p_\delta^+}\end{aligned} \tag{2.5}$$

where the terms are labeled as such: Mean/Viscous, Reynolds Shear Stress Production, Normal Stress Production, Energy Flux, Turbulent Diffusion, and Pressure Diffusion, respectively. Also, the limits on the integrand are from 0 to the boundary layer thickness, δ, or δ_{99} in this case.

It is important to note three characteristics about equation 2.5. First, Walsh *et al.* had a few typos in their equation 8 in [63]; namely, the square in the first term, and the wall coordinates of q (i.e., the plus (+) sign signifying wall coordinates) in the fourth term were missing. Second, the last two terms (Turbulent and Pressure Diffusion) are found to be negligible [63], and are henceforth removed from the equation and/or calculations in the present study. Lastly, the nature of the equation is to compute the values in physical coordinates, followed by converting to wall coordinates with $TS''/\rho u_\tau^3$. This arises from the nonlinearity of x and y when converted into the respective wall coordinates, x^+ and y^+. For clarity, Eq. 2.5 is explicitly written in physical coordinates here

$$\begin{aligned}\int_0^\delta S'''\{y\} = S''\{\delta\} \approx \frac{\rho}{T}\Bigg[\nu\int_0^\delta (\partial U/\partial y)^2 dy - \int_0^\delta (\overline{uv})(\partial U/\partial y)dy \\ - \int_0^\delta \left[\overline{(u^2)} - \overline{(v^2)}\right](\partial U/\partial x)dy \\ - (d/dx)\int_0^\delta U(1/2)\overline{(q^2)}dy \\ - (1/2)\overline{v_\delta\left[(u_\delta^2) + (v_\delta^2) + (w_\delta^2)\right]} - \overline{v_\delta p_\delta}\Bigg]\end{aligned} \tag{2.6}$$

Justification for the removal of the turbulent and pressure diffusion terms in Eq. 2.5, besides just the relative magnitude, is also due to their inability to be measured. The subscript δ in these two latter terms defines the measurements are taken at the *instantaneous* boundary layer location, and at any given instance the boundary layer location will fluctuate. Supposing one could use the average location of the boundary layer, the boundary layer thickness, δ_{99}, should not be used. An illustration of this can be seen in Klebanoff [24] on pg. 1147. Here, Klebanoff distinguishes between the boundary layer thickness, δ_{99}, the mean position of the boundary, $\overline{Y}$, and the boundary itself. That is, the reported δ_{99} is the time averaged $u/U_\infty = 99\%$ location of the boundary layer, and *not* the average boundary layer thickness, $\overline{Y}$. Looking more specifically at the last term, currently there is no means of measuring the instantaneous pressure out near the freestream – wherever that may fluctuate.

Finally, Walsh *et al.* [63] shows how $(S''\{\delta\})^+$ can be brought into terms of the dimensionless dissipation coefficient, C_d, by

$$C_d = \frac{TS''}{\rho U_\infty^3} = (S''\{\delta\})^+ \left(\frac{C_f}{2}\right)^{\frac{3}{2}} \tag{2.7}$$

where skin friction coefficient, C_f, is defined by

$$C_f = \mu \frac{dU}{dy}\bigg|_w \tag{2.8}$$

with $dU/dy|_w$ found methodically, and described later in chapter 4.

2.1 Previous Experimental Studies on Bypass Transition

The following is literature that has lead up to the current work. It is broken up by categories: (1) Influence of free stream turbulence intensity on the transistion process, (2) Measurements of entropy generation rate in bypass transitional flow, and (3) Simulated entropy generation of bypass transitional flow. In the end they come together in order for this work to stand on its own.

2.1.1 Influence of Free Stream Turbulence Intensity on the Transition Process

In order to achieve bypass transition the freestream turbulence intensity (FSTI) must be at an elevated level (>3%). The process of bypass transition has been shown by Dunham [10], Abu-Ghamman and Shaw [1], and Mayle [32] to be heavily dependent on the freestream turbulence intensity (FSTI), and when the FSTI is high enough ($>\sim 3\%$) very little of the transition process relies on the pressure gradient.

McIlroy and Budwig [37] recorded laser doppler velocimetry (LDV) measurements in 2 components within the INL MIR flow system. Their representative model was a flat plate (the same plate reused in the current study) that portrayed the first 1/3 of a high-pressure turbine blade, with and without realistic roughness. An active (and passive) turbulence generator (TG), modeled after the input from Gad-el-Hak and Corrsin [12], brought the FSTI up to an order of $\sim$7% the freestream flow. A trip made from an array of dowel pins near the leading edge of the plate represented the same flow conditions achieved from film cooling of turbine blades. Both the FSTI and the trip resulted in the flow transitioning to a turbulent boundary layer, yet the heavy favorable pressure gradient, in a sense, "relaminarized" the boundary layer in both the smooth and rough cases. The results from the LDV data were

time averaged velocities, and Reynolds normal and shear stresses. The current study requires instantaneous readings of velocities over an entire flow field.

2.1.2 Measurements of Entropy Generation in Bypass Transitional Flow

The first real look into measurements of v' (and therefore $\overline{uv}$) performed within the viscous sublayer with highly favorable pressure gradients were done by McEligot and Eckelmann [35]. Their research provides v' data at locations of $y^+ = 5, 7, 10, 15, 25$ in an oil channel where measurements were made from a "X" probe hot-wire anemometer - along with simultaneous measurements of a wall shear stress sensor. This particular data set was the basis of a further study by McEligot et. al. [34] finding the contribution of entropy generation rate in negligible and favorable pressure gradients.

A flat plate study representative of a turbine blade was performed at the Stokes Research Institute at the University of Limerick. A team of researchers (Walsh *et. al.* [59], Walsh and Davies [60], Nolan *et al.* [40], Walsh *et al.* [64], Walsh and McEligot [61][62]), and Nolan and Walsh [39], under the direction of Walsh, have looked at the careful measurements of S‴ and S″ using hot wire, hot film, and Particle Image Velocimetry (PIV) in such flows as laminar, transitional, and turbulent - as well as compressible and incompressible. This data set was acquired over a set number of turbulence intensities, Mach, and Reynolds numbers. The accuracy of the PIV system was able to reach $y^+ >\sim 10$, achieve gradients of u and v, and apply them to the approximate entropy generation equation defined in equation 2.4. In support of this dataset, extensive DNS solutions have been computed by Nolan and Zaki [41] (more in the next Section, 2.1.3).

2.1.3 Simulated Entropy Generation of Bypass Transitional Flow

Several DNS studies have taken the approach to separate out different parts of the flow structures within a boundary layer. In transitional flow the field is patchy with

a mix of turbulent and laminar spots [49] (See Figure 1.1), which are two completely separate kinds of flow. Depending on what measurements and/or information is needed from a given flow condition, an engineering approach may be to take an average across the entire flow; with the downfall of information about pointwise measurements being lost. On the range of the micro-scale (i.e., any singular location in space and time) any two locations within the flow will behave differently from each other – specifically in transitional flow. To help with the prediction of bypass transition and these above mentioned differing flow structures, Brandt *et al.* [6], and Zaki [68] employed DNS data with an initial laminar boundary-layer upstream boundary-condition that tracks different energy streaks above and within the boundary layer during transition.

Walsh *et al.* [61] utilized a DNS data set to show entropy generation rate occurring mainly in the viscous layer of wall bounded flow. As well, Reynolds numbers are relatively independent from flows with minor pressure gradients. This specific viscous sublayer (i.e., from DNS calculations) was usually on the order of 1-2 mm. This shows the need for high resolution measurements within the viscous sublayer.

It was found in the study of bypass transition by Zaki and Durbin [67] through simulations of low- and high- continuous eddy frequency modes, that the low-frequency mode penetrates the boundary layer shear layer and produces turbulent streaks, by means of the lift-up mechanism. In the high-frequency mode the eddies however remain within the freestream and do not penetrate the boundary layer shear. Further, Zaki and Durbin [68] observed the impact of pressure gradients on bypass transition, and found that the deceleration of the flow reduces the length needed down the length of the plate for the turbulent streaks to begin to form in the boundary layer.

Liu *et. al.* [29, 30] utilized DNS to look specifically at the interaction between the turbulent streaks forming within the transitional region of the flow, and the Tollmien-Schlichting waves. They discovered that there exist a balance between the instability

(though stable nature) of the T-S waves, and a secondary more enhanced instability. These two instabilities oppose one another, and determine the outcome of turbulent streaks forming sooner or later.

Computational fluid dynamics (CFD) was utilized at the University of Idaho to help predict the onset of bypass transition by using various RANS models. Ghasemi *et al.* [14] and George *et al.* [13] all found that the RANS models, heavily used in CFD, either under shot the onset of transition or over shot the entropy being generated when compared to a similar DNS computation. George mentions that the $k-\omega$ 4-equation model came the closest to predicting transition behavior of the boundary layer as the DNS had done.

2.2 Needs and Justification

The above mentioned work by Dr. Walsh's team at Stokes Research Institute at the University of Limerick have shown the laminar region has significant entropy generation, more than was previously thought. Also, free stream turbulence intensity effected the laminar boundary layer, not only by shortening its overall length, but by producing a rate of entropy generation, locally, by the influence of low and high speed streaks on the time-averaged flow. Satisfactory agreement was found between well established semi-empirical correlations and that of the measurements taken by the team at Stokes Research Institute – more specifically, in the regions of laminar flow with low free stream turbulence intensity and that of well developed turbulent flow. Lacking still is the agreement between the transitional region and the said semi-empirical correlations. From this specific work three main scientific questions have arisen as fundamental difficulties with the prediction and measurements of S'' and S''': the onset, duration, and entropy generation rate of the transition region. All must have sufficient data within $y^+ < 5$.

Chapter 3

Experimental Methods

The following is a compilation of the equipment, settings, and procedures used in the current work.

3.1 Matched Index of Refraction Flow Facility

The Matched Index of Refraction (MIR) Flow Facility located at the Idaho National Laboratory (INL) in Idaho Falls, ID is the largest in the world – which has the advantage of being able to obtain highly detailed information about many flow conditions - all while not interfering with the flow itself. Stoots [51] provides details of this system, also see Fig. 3.1. The MIR utilizes the matched index of refraction [7] between quartz and mineral oil to remove any visual effects from the bending of light rays (refraction) through characteristic models in order to resolve flow patterns optically in or around the models themselves.

There is approximately 3,000 gallons of oil in the closed loop of the MIR, and an axial pump is able to push the fluid at approximately 10,000 gpm. The current working matching temperature of the mineral oil to quartz is $25.156°C$, and the MIR temperature control loop was able to maintain this temperature within $\pm 0.05°C$. This was accomplished by drawing approximately 300 L/min of the oil from the main tunnel and running the fluid through various heat exchangers and/or heat stacks. A traversing mechanism with accuracy in position within ± 0.005 mm moved the camera optics, utilized in the MIR measurement techniques, in all three directions, either manually or automatically. The traverse allowed for the entire centerline plane (xy-plane) of the test section of the MIR to be imaged – with the exception of two supports that hold the walls of the MIR test section where the optics were blocked (not shown in Figure 3.1). As mentioned above, the working fluid of the MIR is a

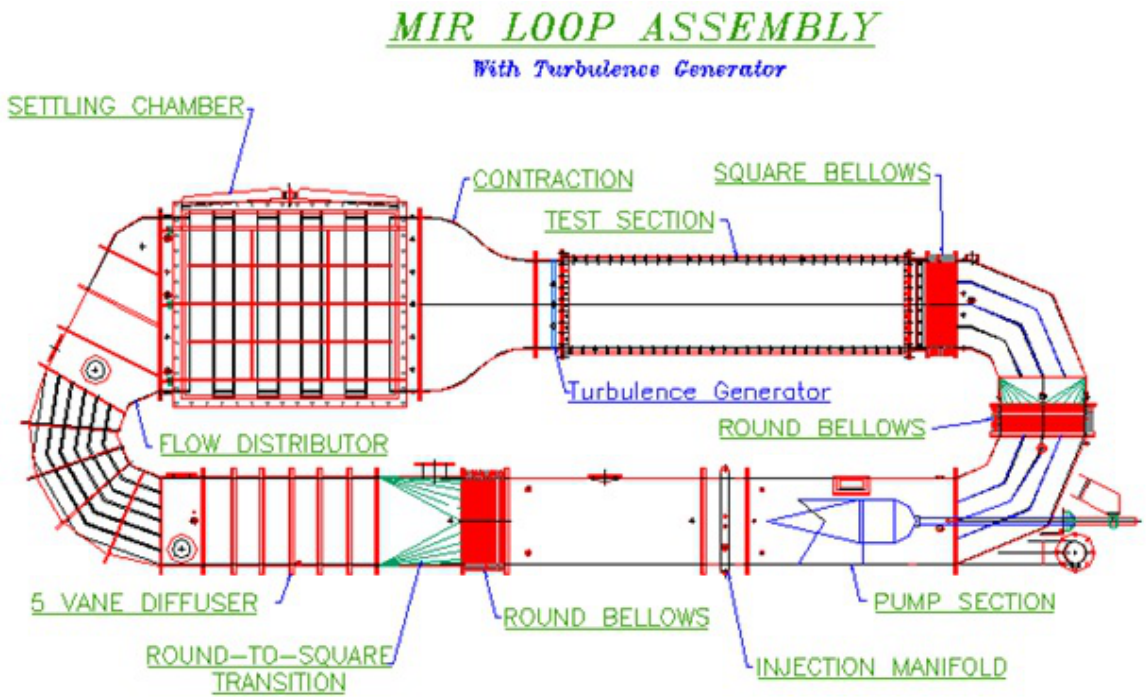

Figure 3.1: Schematic diagram of the MIR Flow Facility

light mineral oil with fluid properties – and corresponding uncertainties – by Budwig and Westin [8] at the MIR matching temperature of $25.156°C$ are shown in Table 3.1.

3.2 Experimental Apparatus – Flat Plate

Figure 3.2 shows the CAD rendition of the flat plate apparatus within the test section of the MIR. Flow is going from right to left. The CAD model shows a cut away of the test section, where the three windows on each side of the tunnel for obtaining optical data are also shown. The optical windows are made of soda-lime float glass for a highly smooth and flat surface. Quartz sections of the flat plate are visible within each of the three windows (transparent sections of the plate). The coordinate axis followed the traditional right hand rule (as shown in Figure 3.2), and was held at the center of the leading edge to the plate - with streamwise (and upstream) as x, normal

Table 3.1: Light mineral oil fluid properties in the MIR.

Parameter	**Value**
Matching Temperature	$25.156°C$ $\pm 0.005°C$
Fluid Density, ρ	0.830 [g/mL] ± 0.00024 [g/mL]
Kinematic Viscosity, ν	$1.32x10^{-5}$ $[m^2/s]$ $\pm 7.8x10^{-8}$ $[m^2/s]$
Index of Refraction	1.458
Maximum flow in empty tunnel	1.7 [m/s] 10,000 gpm

to the top surface of the plate as y, and spanwise to the tunnel as z.

The setup of the flat plate had three different flow configurations, each adding more complexity than the last. In the first flow configuration, as seen in Figure 3.3a, the flat plate is situated in an empty tunnel in order to have a very low free stream turbulence intensity and negligible "zero" pressure gradient. This flow configuration was utilized to basically calibrate the experimental setup of the tunnel, as the flow was quiet and predictable it was easily analyzed against common theoretical flows such as the Blasius solution for laminar flow. In Figure 3.3b the plate had the same configuration as the first with the one addition of a turbulence generator (TG) which was an array of 21 horizontal round bars with 12.7 mm diameter and 25.4 mm pitch. The TG has the option of being blown (i.e., small holes injecting fluid into the bulk flow from a secondary controlled loop), but it was observed by McIlroy and Budwig [37] to have more turbulent contribution if the TG was held passive to the flow. In other words, the

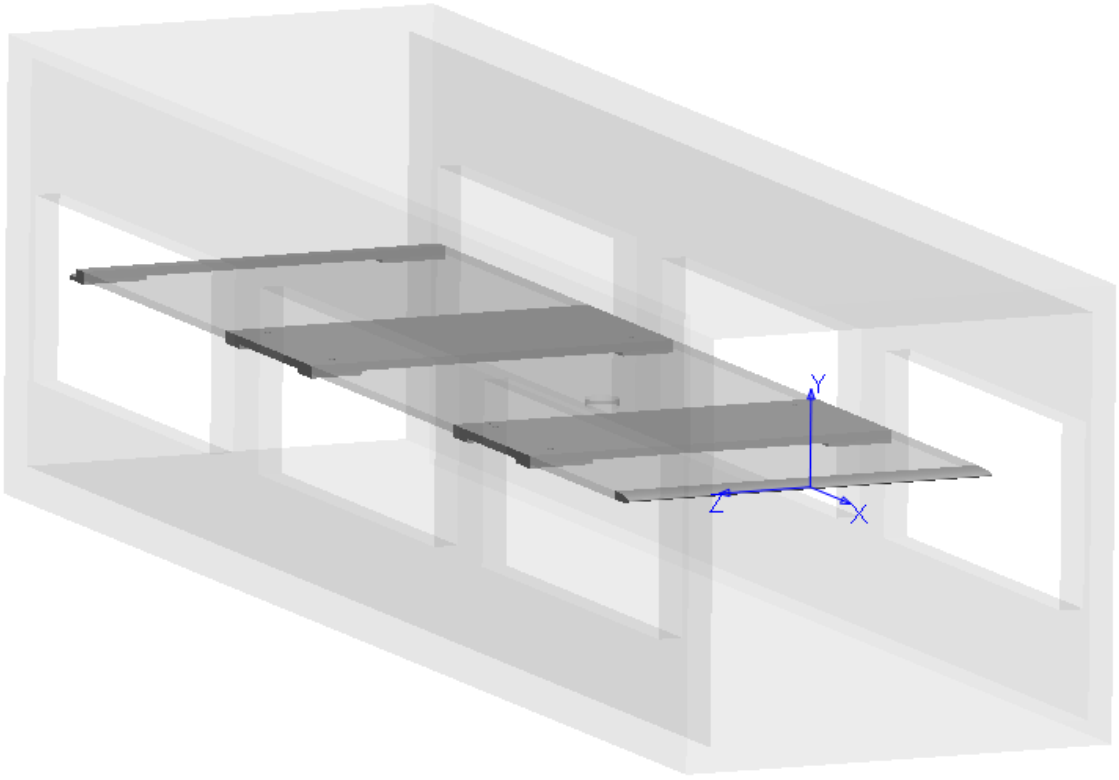

Figure 3.2: Geometry of the flat plate in the tunnel, with the origin at the leading edge of the plate. Flow is from going from right to left.

TG bars were only present, and no auxiliary flow was injected. Furthermore, in Figure 3.3c the TG was still present, and an adverse pressure gradient was installed above and below the experimental plate (for symmetry of the flow conditions) in the form of flat aluminum plates. This began with a bell-mouthed curve that contracted the flow down, which ended just at the leading edge of the flat plate. The bell-mouthed curve then transitioned immediately and linearly diverged at an angle of 3.85°. In summary, the datasets are henceforth titled: (a) Zero Pressure Gradient without Turbulence Generator (ZPG without TG), (b) Zero Pressure Gradient with Turbulence Generator (ZPG with TG), and (c) Adverse Pressure Gradient with Turbulence Generator (APG with TG).

Within the three flow configurations there are common features to the experimen-

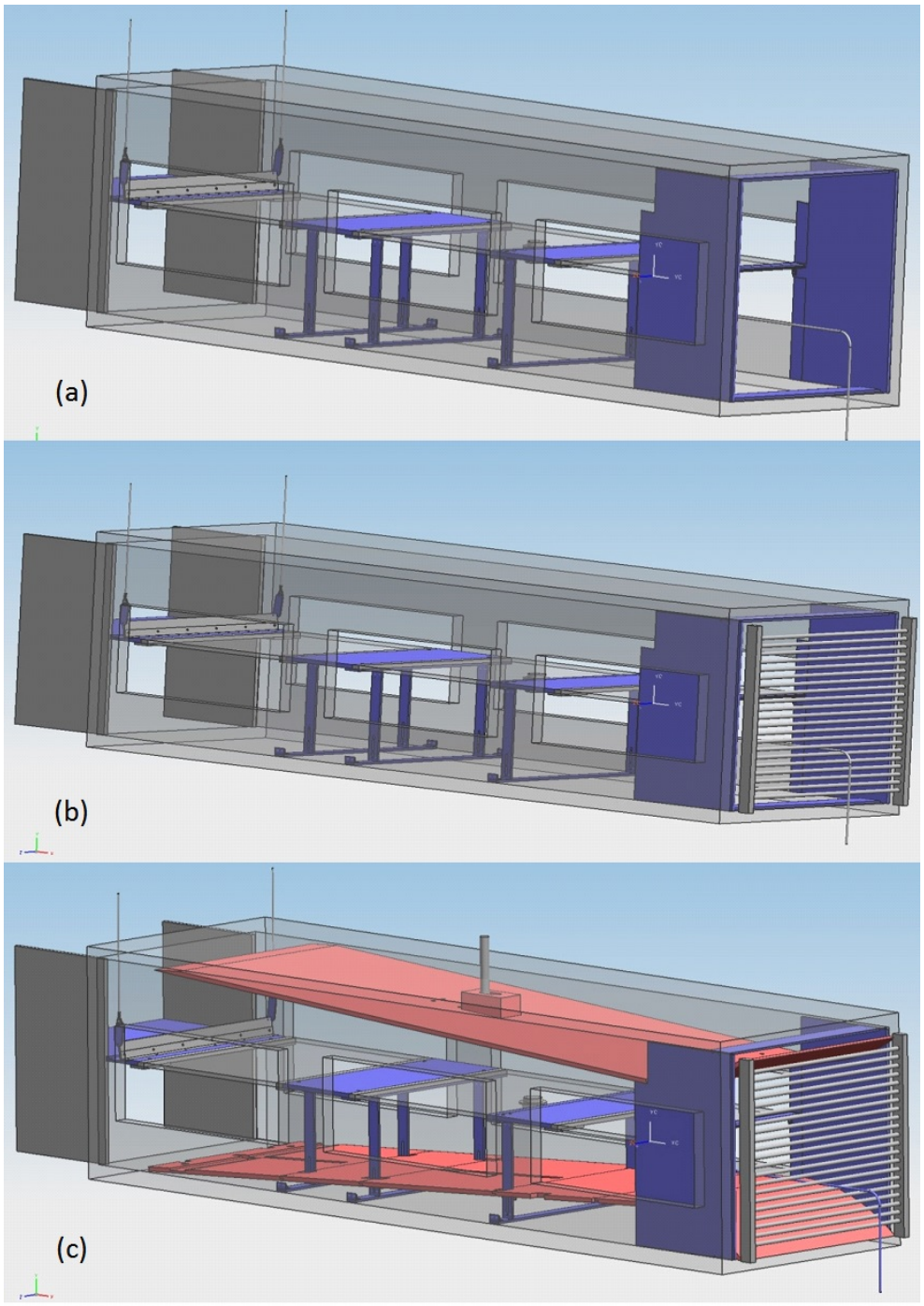

Figure 3.3: Flat plate configurations of the three tests performed on the flow. (a) ZPG without TG (b) ZPG with TG (c) APG with TG. Flow is going from right to left.

tal setup. First, majority of the support for the plate was provided from underneath by low profile aluminum bars. With the exception of the leading and trailing edge of the plate that were supported by 6.35 mm thick aluminum plates that stood vertically in the tunnel from top to bottom, and supported the plate at the midsection. Second, a 5 cm aluminum leading edge design was defined by a symmetrical ellipse that ended just over its minor axis (about 2.5 cm downstream), and continued downstream as a flat plate for another 2.5 cm – at which point the first quartz plate began (i.e. the first measurement location). This design was chosen as both Frannson [11] and Hanson *et al.* [17] show the pressure distribution from leading edge effects at a minimum between 1 and 1.5 lengths of the ellipsoidal part of the leading edge. Third, a flap mechanism at the downstream side of the plate helped equalize the cross sectional areas between the top and bottom of the plate. Lastly, in all three experimental configurations a local seeder was held just at the centerline (xy-plane), leading edge of the flat plate where highly seeded oil was injected at a low flow rate in the hopes of entraining seeding particles within the boundary layer of the flow (see Section 3.3 for more info).

3.3 Local Seeding System

The MIR tunnel was seeded with 12 micron (on average) hollow glass spheres that are silver coated. Due to the interface between freestream flow and boundary layer on the flat plate the seeding becomes sparse within the boundary layer. There was a need for the seeding particles to enter the boundary layer directly at the leading edge, and it was observed that Kähler et. al. [23] used a local seeder in his work. A small 6.35 mm ID tube was installed directly at the leading edge of the plate (see Figure 3.4), and highly seeded oil (at matching temperature) was drawn at an extremely low flow rate from a vat within a secondary loop (not shown). The vat was temperature controlled by the secondary loop that was completely separated –

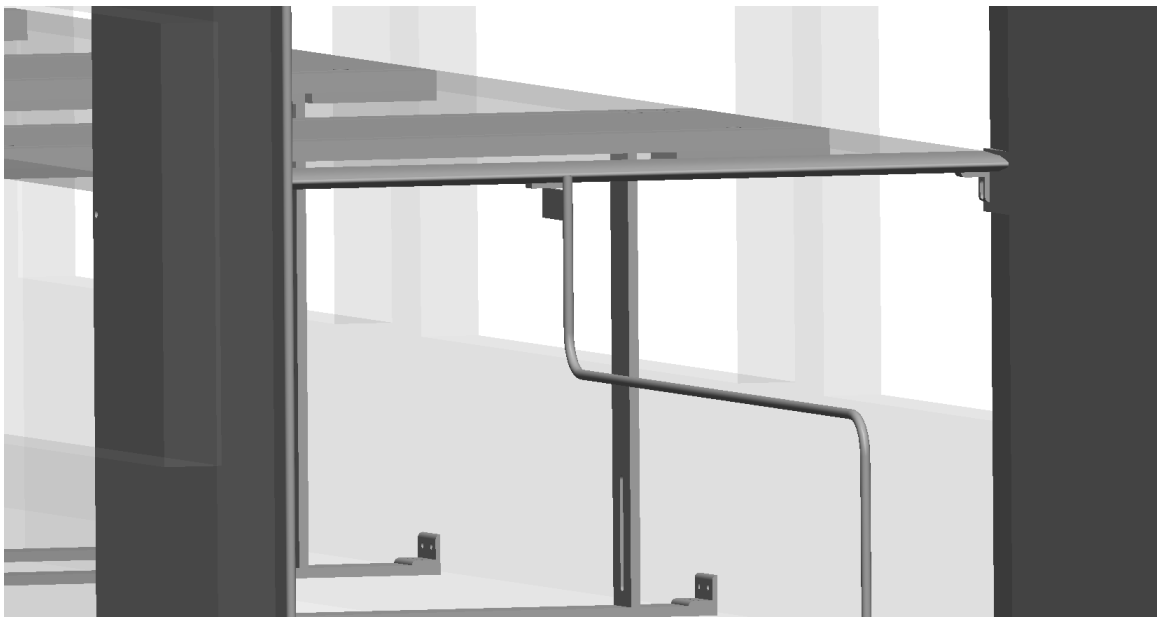

Figure 3.4: Local seeder just at the leading edge of the flat plate.

thermally and hydraulically – from the main loop shown in Figure 3.1.

The local seeding system worked very well for the ZPG without TG flow, but when the TG was installed for the later two flow conditions the turbulent eddies broke up the stream of fluid coming from the local seeding system within the first 150 mm to 200 mm of flow atop the plate. This caused a low seeding density within the boundary layer on these two flow configurations, and lead to the need to use the measurement technique Particle Tracking Velocimetry (PTV) in this region instead of PIV (see more in section 3.5).

3.4 Sample Size

Turbulence measurements need a relatively large data set in order to resolve actual turbulence quantities and not just artifacts. A procedure put forth by Uzol and Camci [56] resolves an appropriate number of samples needed to accurately address this issue. A large number of samples were taken (in this case 10,000 image pairs), followed by 100 subsets that were chosen at random from the overall (e.g. 100 random

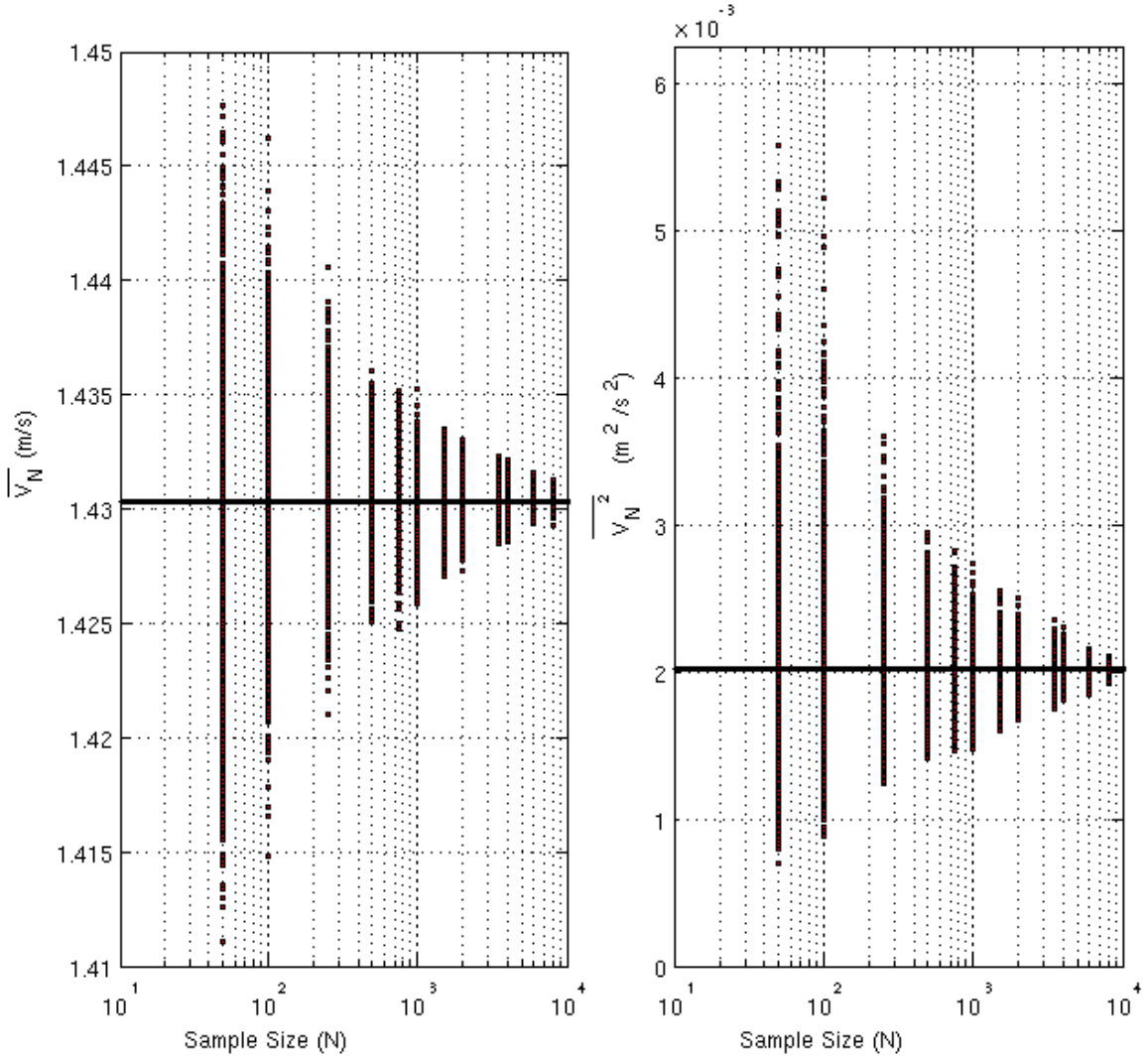

Figure 3.5: Convergence study for PIV and PTV sample size.

sets of 250 image pairs taken from the overall 10,000 image pairs), and, finally, each subset is analyzed for mean and turbulence quantities. This is then repeated by an incrementally increasing sample size (while the number of subsets is held constant) that are also randomly taken from this overall sample, up to the total 10,000 image pairs (where the 100 subsets is ignored in this last dataset as the mean and turbulence quantities would not change).

This procedure was then taken one step further than the Uzol and Camci algorithm [56] in the sense that the study was done over the entire FOV, and not just at a

randomly selected location. After running the aforementioned algorithm over the entire FOV the location in the FOV that took the longest to converge was selected as the "worst case scenario". This made certain the convergence was met for the entire FOV by satisfying this worst case scenario. This means that for most of the FOV the sample size went above and beyond the needed sample.

Looking now specifically at this worst case scenario location in the FOV the mean from the 10,000 image pairs was deemed the "golden" standard, and all other subsets were held against this total dataset. Figure 3.5 shows the velocity mean and turbulent quantity variations, left and right, respectively, for all subsets on a semi-log scale. The chosen convergence ($< 0.3\%$ for the error in velocity measurements, $< 6.1\%$ for the error in turbulence quantities, and hard drive size considerations) was selected at 4,000 image pairs, and all subsequent data sets were set at a sample size of 4,000.

3.5 Particle Image Velocimetry/Particle Tracking Velocimetry

Velocities, instantaneous gradients, time-averaged gradients, and turbulence measurements were obtained using LaVision's FlowMaster and a Nd:YAG green laser (532nm). By using transparent quartz at the same index of refraction as mineral oil, the green laser sheet shown directly through the flat plate from below, and avoided reflections on the surface of the plate. This gave unaltered, whole field, vector maps on the centerplane (xy-plane) of the flat plate that have immense amount of information needed for the various gradients in the entropy calculations very near the plate. The images of the flow were recorded at two levels: large field of view (LFOV) and mezzo field of view (MFOV), as depicted in Figure 3.6; with the vertical (plate normal) length of the images being $\sim$130 mm and $\sim$7 mm, respectively. As a further note, the LFOV was recorded at every location down the plate (i.e., the entire cen-

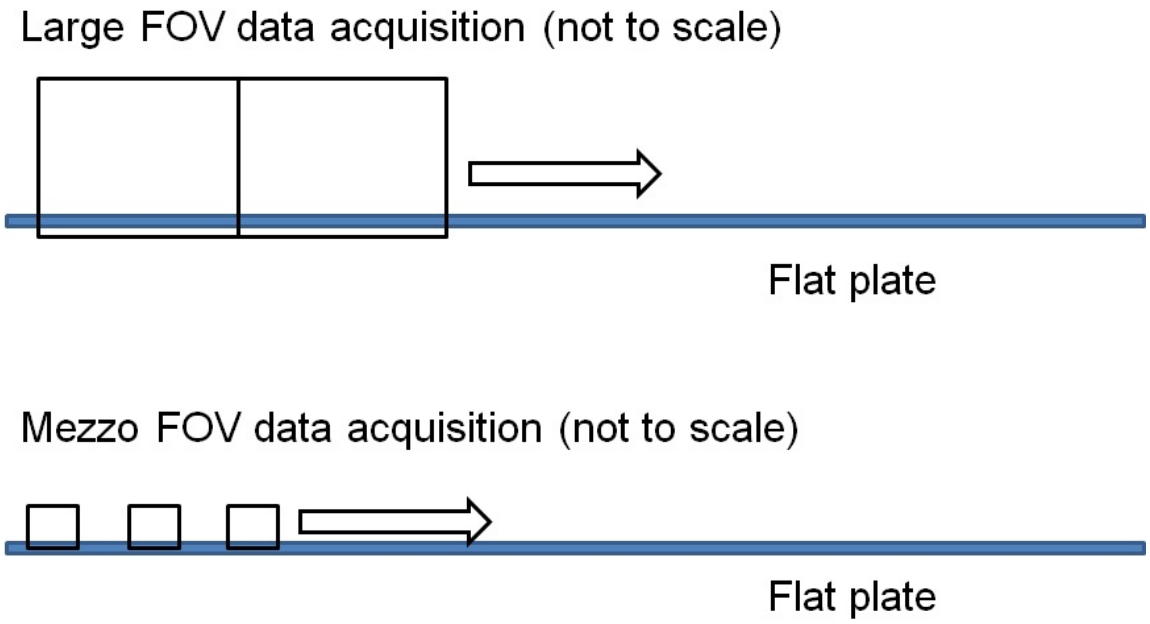

Figure 3.6: Data Acquisition locations for both large and mezzo fields of view. Not to scale.

terline plane of the plate was recorded with the exception of the supports on the test section), while for the MFOV scale, the images were recorded at every other location.

In order to have an appropriate particle displacement within both the large and mezzo field of view a simple calculation of ratios was performed

$$dt = \frac{FOV_x}{U_{max}} \frac{\Delta x}{\#px} \tag{3.1}$$

where FOV_x is the calibrated image dimension in the x direction, U_{max} is maximum observed velocity, Δx is the desired pixel displacement of the particles in an IW, and #px is the overall number of pixels on the camera sensor in the x direction. The dt in the LFOV varied respective of the flow conditions of each case study, from 660 to 1200 μs. Also, due to the high deceleration of the flow in the APG case, the dt was varied within the case itself, from 660 - 890 μs.

The LFOV was processed using PIV (more specifically the cross correlation method), and was able to capture freestream conditions, boundary layer location, and integral parameters of the wall bounded flow. Initial processing was done with 128 x 128 pixel interrogation windows (IW) followed by one iteration of 64 x 64 pixel IW, and then finally by two iterations at 32x32 pixel IWs. A 75% overlap of the final pass was used for all PIV processing. This gave a final pass, velocity vector, grid of 8x8 px. Table 3.2 shows an overview of the PIV flow parameters.

The MFOV was processed using PTV (due to its relatively low seeding density), and captured high resolution images very near the wall in order to resolve the shear stress at the wall. This small scale image was also utilized to resolve the various gradients in the flow on the order of the Kolomogorov length scale, η. An initial PIV algorithm was passed over the MFOV to achieve an initial idea of the flow conditions. This gives a best "guess" for the PTV to take place. The velocity vector output from the MFOV PIV is then utilized as the start of the PTV algorithm. The PTV looked for particles sized 2-6 px in apparent diameter within both frames, and output a velocity vector where successful. Velocity vectors from PTV are reported on an unstructured grid; therefore there was a need to interpolated to structured grid in order to calculate time averaged quantities at a single location. The 8x8, center-to-center grid was chosen for the final size of the PTV output. This allowed for the distances between velocity vectors to be on the same order of magnitude as the Kolomogorov length scale. The interpolation used nearest neighbors and a third-order curve fit to snap the vectors to the center of each grid location. In total, approximately 2,000 vectors were kept *at each grid center* from the 4,000 taken. Table 3.3 details the parameters used in PTV of the MFOV.

This smaller image scale was able to reach deep into the viscous sublayer and measure instantaneous and averaged quantities. The dt on the mezzo scale varied across all datasets from 36 μs to 200 μs. Specifically though, within the APG with

Table 3.2: Large field of view PIV flow parameters for all three flow conditions.

Parameter	**Value**
Image Size	172 mm x 130 mm (1200x1600 px)
Typical particle density (diameter)	0.03 ppp (3.25 px)
dt	ZPG without TG: 850 μs ZPG with TG: 1200 μs APG with TG: 660-890 μs
Interrogation Window (# of passes)	128x128(1) 64x64(1) 32x32(2)
% Overlap on Final Pass	75%
Post-Processing	Remove vector: $Q < 1.3$ Universal outlier detection
Final LFOV PIV Grid (px)	0.889 mm (8)

Table 3.3: Mezzo field of view PTV flow parameters for all three flow conditions.

Parameter	**Value**
Image Size	10 mm x 7 mm (1200x1600 px)
Typical particle density (diameter)	0.005 ppp (3.5 px)
dt – high	ZPG without TG: n/a ZPG with TG: n/a APG with TG: 99-200 μs
dt – low	ZPG without TG: 36 μs ZPG with TG: 144 μs APG with TG: 49-115 μs
PIV Initial Passes (# of passes)	128x128(1) 64x64(1) 32x32(2)
% overlap on Final PIV Pass	50%
PIV Post-Processing	Remove vector: $Q < 1.3$ Universal outlier detection Fill-up all
PTV Particle Image Diameter	2-6 px
Final MFOV PTV Grid (px)	0.05 mm (8)

TG MFOV the flow was moving too fast near the leading edge to utilize only one dt at each location. Therefore, two time steps were selected – one for the upper part of the image (faster fluid motion, away from the plate), and a second for the lower part (slower fluid motion, closer to the plate). Both datasets were taken without moving the camera before proceeding. As an example, the current study was able to capture ∼18-20 data points of mean flow within the viscous sublayer ($y^+ < 5$) of the wall bounded flow (see Figure 3.7, more on this in Section 4). In order to understand an order of magnitude of size of the sublayer, a $y^+ = 1$ throughout the flow configurations is approximately 10^{-4} m from the plate surface (y-direction).

3.6 Image Calibration

The camera was mounted perpendicular (⊥) to the MIR test section windows, therefore any aberrations (e.g. diffraction) of the image plane is at a minimum – worst case being the corners of the image. Regardless, with the light rays going from one medium to another, and in this case even a third, calibration of the image sensor (pixels) to image plane (inches) was needed. On both levels, the LFOV and MFOV, a calibration plate was submerged in the oil below the flat plate. For the LFOV a LaVision type 7 calibration plate with dot to dot spacing of 5 mm was used to calibrate the image plane. For the MFOV, a μPIV calibration plate was used with dot spacing of 1 mm or less (see Figure 3.8).

3.7 Vibration Control

Running the tunnel at full speed, it was found that the camera mount on the traversing system vibrated slightly, even with an air bladder system elevating the tunnel; more specifically in the MFOV where the overall length was ∼8 mm. It was seen that the vibration time scale was magnitudes larger than the time between

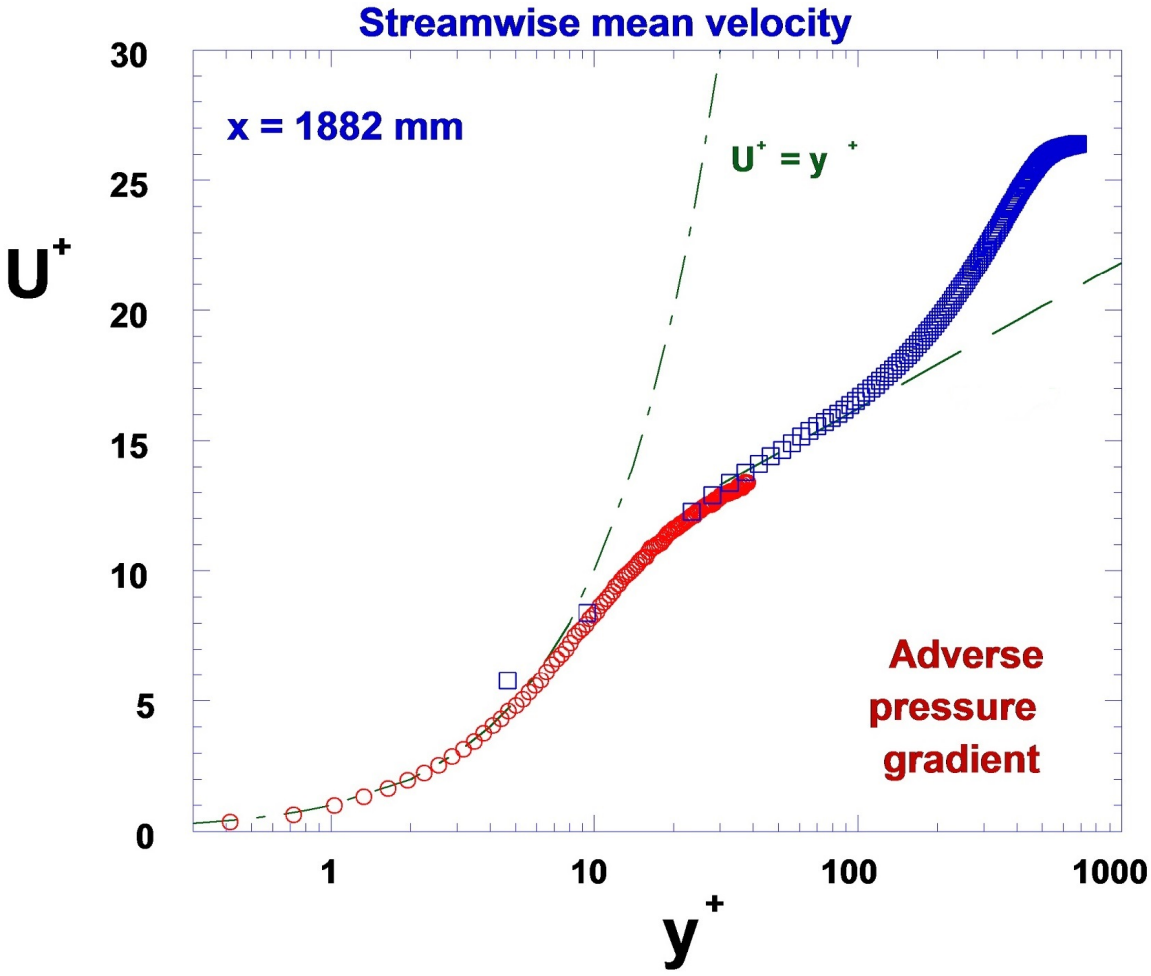

Mezzo FOV: ○
Large FOV: □

Figure 3.7: Velocity Profile near downstream of plate [33]. Plot is shown for illustrative purposes to see how much data was achieved within the viscous sublayer (i.e., 18-20). More on this in Section 4.

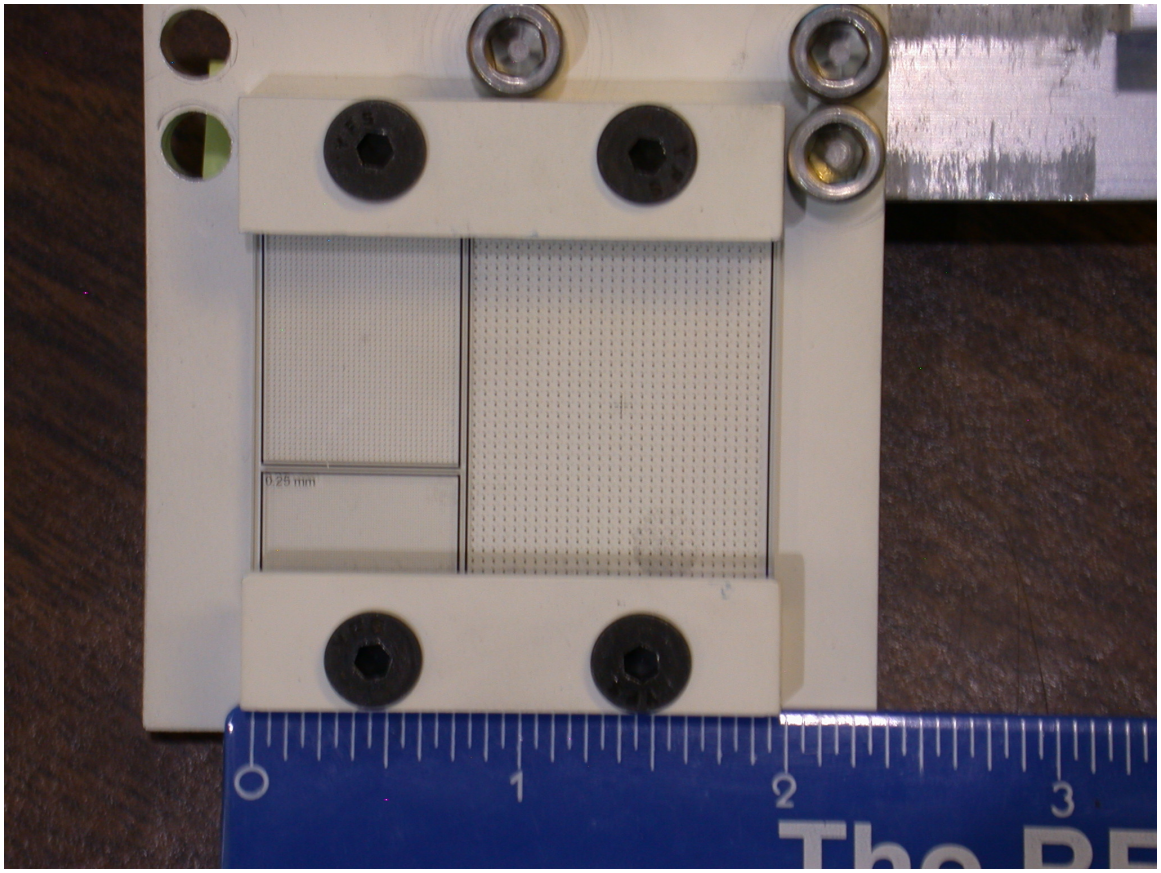

Figure 3.8: Calibration plate for mezzo field of view. Scale in inches.

image pairs, dt, therefore the vibration correction was handled after data acquisition. A PIV algorithm within the LaVision DaVis software was used to remove the shifting of image pairs from one pair to another by utilizing the surface of the plate as the image structure that should not move between images. The surface of the plate was identified by small particles that rested on the plate surface, and formed a bright band of light in the image – as the plate itself was transparent from the refraction matching. The top of the plate can be seen in Figure 3.9, where the MFOV raw image is seen on the left and the average intensity count across the horizontal is seen on the right. This shows that the bright band of light at the plate surface is a perfect candidate for the PIV algorithm to align the images to the same location throughout the image set.

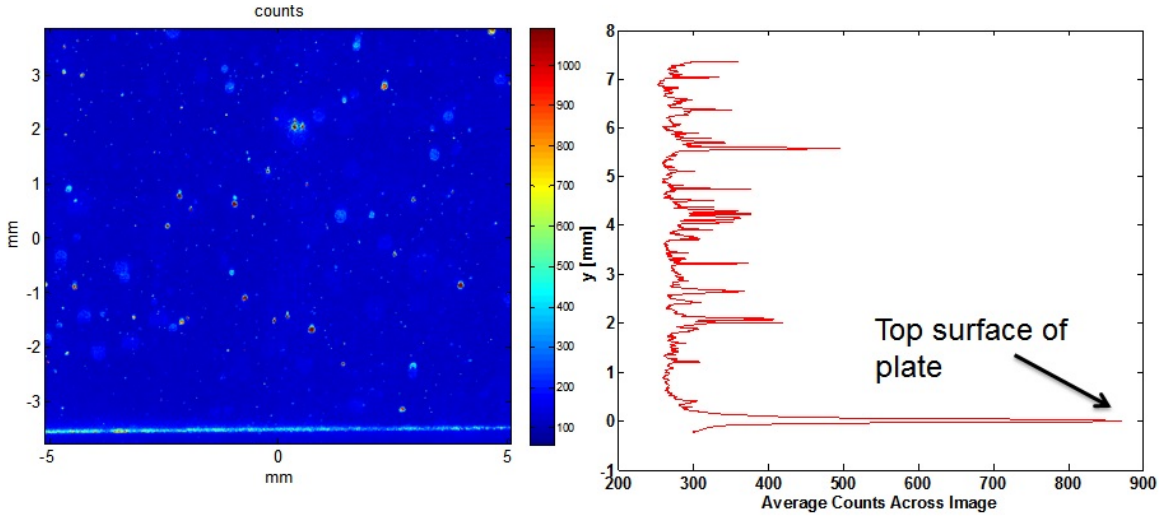

Figure 3.9: Plate identification used in both LFOV and MFOV to align datasets and remove vibration of the camera system. Example image shown is from the MFOV dataset.

Chapter 4

General Flow Conditions

4.1 Freestream Velocity

As freestream velocity, U_∞, is such an important measurement in fluid flow over a flat plate it will be discussed first. The current work used a method similar to that of Nolan and Zaki [41] to find the freestream velocity. At each individual x location, freestream velocity was recorded along the wall normal direction whenever $|dU/dy| < 0.002$. After which, the values recorded were then averaged over the y-direction. This method of finding freestream velocity was then repeated at each x location giving the profile $U_\infty(x)$. In mathematical form the measured freestream velocity, U_∞, is defined by the following two equations

$$U_\infty = \frac{1}{j}\sum_{1}^{j} U(j) \tag{4.1}$$

where j is the index up to the number of nodes in the y direction and $U(j)$ is

$$U(j) = \begin{cases} U(j) = U(j), & \text{if } |dU/dy(j)| < 0.002 \\ U(j) = NaN, & \text{otherwise} \end{cases} \tag{4.2}$$

where dU/dy is found with a simple central differencing scheme about the point of interest. It is also important to point out that equation 4.1 is computed by ignoring any reference to "Not a Number" (NaN) that are present in the gathering of U(j) in equation 4.2. Further, index j is the size of all real numbers in U, ignoring NaNs as well.

4.2 Streamwise Profiles

Freestream velocity was utilized to calculate the boundary layer growth, δ_{99}, and integral parameters, δ^* and θ, of all three flow conditions. With the boundary layer thickness defined as the point, normal to the wall, where the velocity, u(y), is essentially 99% of the freestream streamwise velocity

$$\delta_{99} = y_j \qquad \text{when} \qquad \frac{U(y_j)}{U_\infty} = 0.99 \qquad \text{with} \qquad j = 1...n \tag{4.3}$$

where again j is the wall normal index, and n is the maximum nodes in the wall normal direction. The integral parameters displacement, δ^*, and momentum, θ, thicknesses are defined by

$$\delta^* = \int_0^\infty (1 - \frac{U(y)}{U_\infty})dy \tag{4.4}$$

$$\theta = \int_0^\infty \frac{U(y)}{U_\infty}(1 - \frac{U(y)}{U_\infty})dy \tag{4.5}$$

where the integration limit, ∞, can be dropped and replaced with δ_{99} from equation 4.3. The freestream velocity and the location of δ_{99} must be deduced from the measured velocity profiles. Also, Equations 4.3, 4.4, and 4.5 are all functions of x, producing their respective streamwise profiles. It is noteworthy that δ^* holds for all incompressible flow conditions, while θ on the other hand only works for flat plate incompressible flow.

The freestream velocity is also utilized in the following equations to further clarify the fluid motion

$$Re_\theta(x) = \frac{\theta(x)U_\infty(x)}{\nu} \tag{4.6}$$

$$Re_x(x) = \frac{xU_\infty(x)}{\nu} \tag{4.7}$$

$$FSTI_x(x) = \frac{U_{RMS}(x)}{U_\infty(x)} \tag{4.8}$$

$$K_t(x) = \frac{\nu}{U_\infty^2(x)} \frac{dU_\infty(x)}{dx} \tag{4.9}$$

where K_t is the acceleration parameter, Re_x and Re_θ are Reynolds number based on position from the leading edge of the flat plate and local momentum thickness, respectively, and lastly the free stream turbulence intensity ($FSTI_x$) in the streamwise direction as related to the x-component of the velocity feild. That is, far enough downstream from the TG, isotropic behavior of the freestream is assumed, and the full equation for turbulence intensity,

$$Tu = \sqrt{\frac{1}{3}(\overline{u'^2} + \overline{v'^2} + \overline{w'^2})}/U_\infty,$$

is reduced to Eq. 4.8 by means of the isotropic behavior, $\overline{u'^2} = \overline{v'^2} = \overline{w'^2}$ [49].

Explicit care has been taken in equations 4.6 through 4.9 to show they are a function of x only, and therefore produce streamwise profiles. Also, since they are based on x only, the values computed are all local values. For example, it is common in the field to hold freestream velocity constant at some upstream location, but in the present work the freestream velocity changes with x location.

The trapezoidal rule was utilized in the numerical integration of Equations 4.3, 4.4, and 4.5. The results from these numerical schemes can be seen on the left side of Fig. 4.1. This left side of Fig. 4.1 shows that the ZPG with TG boundary layer increases at a faster rate than the ZPG without TG case. The TG creates a $FSTI_x$ of $\sim$8% at the leading edge of the flat plate, up from the 0.5% found in the ZPG without TG case. The freestream turbulence provides energy to the boundary layer and "trips" the flow closer to the leading edge; which in turn has an effect on the growth rate of the boundary layer thickness [66]. Likewise, the APG with TG boundary layer grows at an even larger rate than the ZPG with TG as the adverse pressure gradient and turbulent freestream are both present.

The set of data in the last window of the APG with TG case has been removed due

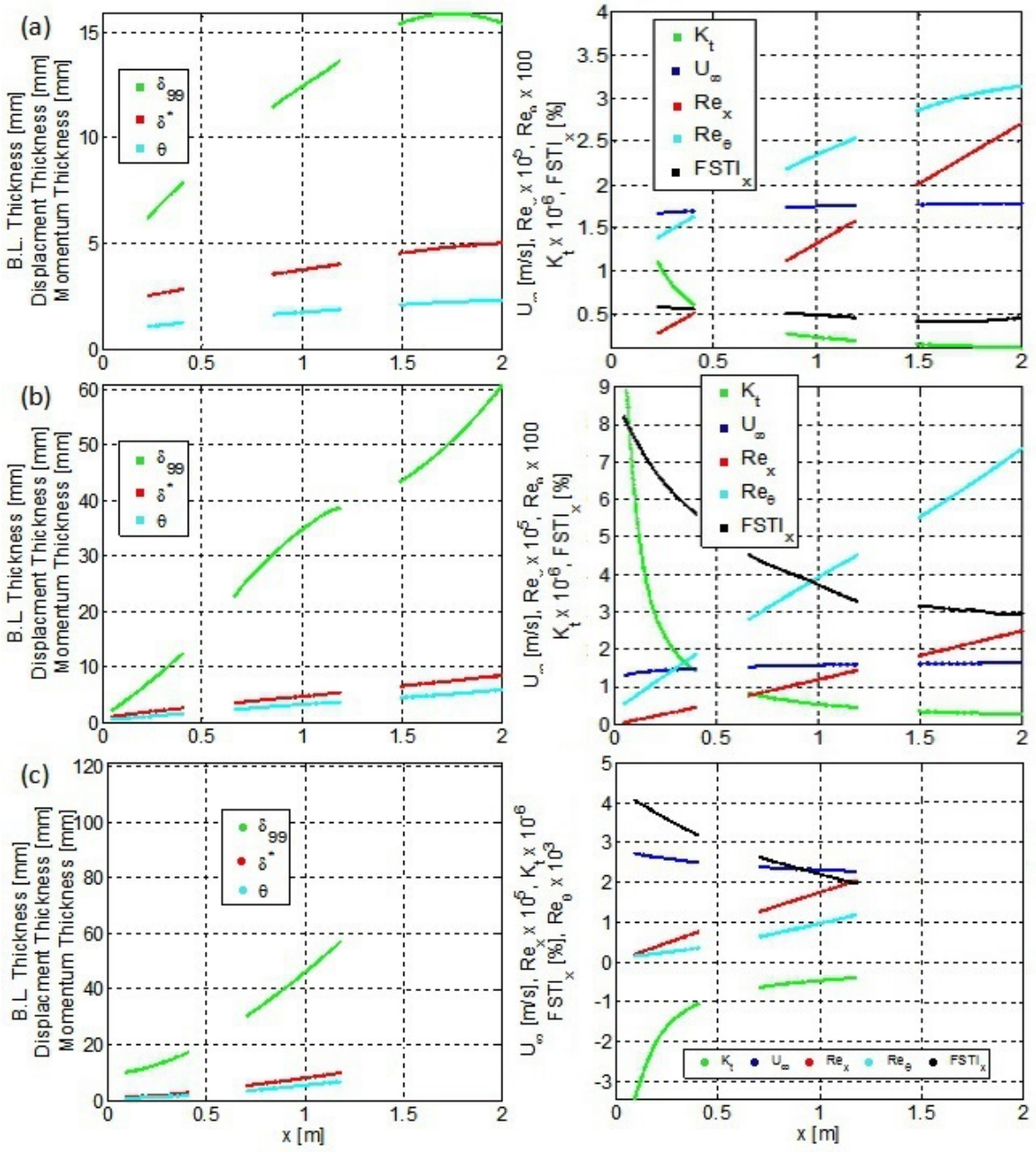

Figure 4.1: Streamwise profiles of measured quantities. Left side: Boundary layer and integral parameters of flat plate flow for three flow conditions. Right side: Freestream velocity, acceleration parameter, Kt, Reynolds number based on distance from leading edge and based on momentum thickness, and freestream turbulence intensity for all three cases. (a) ZPG without TG. (b) ZPG with TG. (c) APG with TG.

to the boundary layer thickness being over sized for the current LFOV. This arises from the inability to obtain the freestream conditions, and therefore the location of the boundary layer. Further, since the integral parameters utilize the freestream velocity – and an integration limit of the boundary layer thickness – they were not calculated for this third window dataset, as well. This was found to be acceptable, as will be seen in later sections, because the transition process for this dataset has already occurred within the first window.

The right column of Figure 4.1 show the various freestream profiles defined earlier. Notice the various "inlet" freestream turbulence intensities. Where for the ZPG without TG case the $FSTI_x$ is well below 1%. This means if any onset to transition is going to occur it will be through the traditional T-S instabilities, presumably. The other two flow conditions (ZPG with TG and APG with TG) are both well above the 1% threshold, and will therefore "bypass" the T-S waves. It is noteworthy that the acceleration factor, K_t, is not constant for the two ZPG cases as the tunnel walls provide a "negligible" favorable pressure gradient within the ZPG flow configurations – actually, there are six viscous boundary layers essentially forming in the closed tunnel: top and bottom of the experiment (the top boundary layer being the one of interest), and on all four walls of the tunnel. Also, the K_t found in the APG with TG case is always negative in sign as the freestream flow has a deceleration.

4.3 Wall Normal Profiles

Figure 4.2 is a representation of the flow at 6 locations (2 per each MIR window – with the exception of the APG with TG flow configuration where the last 2 datasets were removed) down the length of the tunnel. The left side shows the streamwise mean velocity profiles, and their growth outwards away from the plate. The streamwise velocity has been normalized by the local freestream velocity, $U_\infty(x)$. Also, on the left side of Fig. 4.2 is the comparison of Reynolds shear stress down the length of the

plate

$$ReSS = \rho\overline{u'v'} \tag{4.10}$$

which has units of stress. For constant density (which is the present case), ρ can be dropped, and the quantity is normalized by the squared local freestream velocity

$$ReSS = \frac{\overline{u'v'}}{U_\infty^2} \tag{4.11}$$

The Reynolds shear stress plots show that for the ZPG without TG configuration the Reynolds shear stress is at a minimum throughout the boundary layer, but for the ZPG and APG with TG flow configurations the Reynolds shear stress ramps up through the boundary layer and comes back down just near the wall – which satisfies the no-slip condition at the wall where fluctuations go to zero. The contrast between flow configurations stems from the introduction of freestream turbulence in the latter two cases. These freestream turbulent eddies introduce stress on the developing boundary layer very early on in the flow.

The right side of Figure 4.2 shows the streamwise turbulence intensity defined as

$$TI_x(y) = \frac{\sqrt{\overline{u'^2}}}{U_\infty} = \frac{U_{RMS}(y)}{U_\infty(x)} \tag{4.12}$$

and the normal component turbulence intensity as

$$TI_y(y) = \frac{\sqrt{\overline{v'^2}}}{U_\infty} = \frac{V_{RMS}(y)}{U_\infty(x)} \tag{4.13}$$

where the turbulence intensity is similar to that defined in equation 4.8, but a wall normal profile is desired instead of the freestream profile. $U_{RMS}(y)$ and $V_{RMS}(y)$ are the standard time-averaged rms levels of the, respective, streamwise- and normal-velocity components in the wall normal direction, while U_∞ is, again, the local time-averaged streamwise freestream velocity.

The low-level freestream turbulence for the ZPG without TG case of about 0.5%. In contrast, the ZPG with TG case starts out at approximately 8% and decays down to 2.5% by the end of the tunnel. Presumably, both datasets with a TG started out with the same "inlet" $FSTI_x$, but due to the bell-mouthed curve that converged the flow in the APG with TG case, the $FSTI_x$ starts out at around 4% in the first dataset and decays to 2.5% at the end of the plate.

The high turbulence levels within the boundary layer are consistent with boundary layers as seen in McIlroy and Budwig [3]. These relatively high turbulence levels within the boundary layer – fed from the freestream turbulence intensity – near the leading edge are what lead the flow to bypass transition where the Tollmien-Schlichting waves are bypassed [25, 21].

4.4 Blasius Flow as Compared to the Current Work

In order to "calibrate" the entire setup and tunnel, and get a better understanding of the instrumentation the ZPG without TG flow configuration was compared to the Blasius solution of laminar flow at a location near the leading edge. Schlichting [49] cites Blasius [4] , the first student of Ludwig Prandtl, who had the ingenious idea of non-dimensionalizing the distance from the wall with

$$\eta = y\sqrt{\frac{U}{2\nu x}} \tag{4.14}$$

and using η as an input to the Blasius equation

$$f''' + ff'' = 0 \tag{4.15}$$

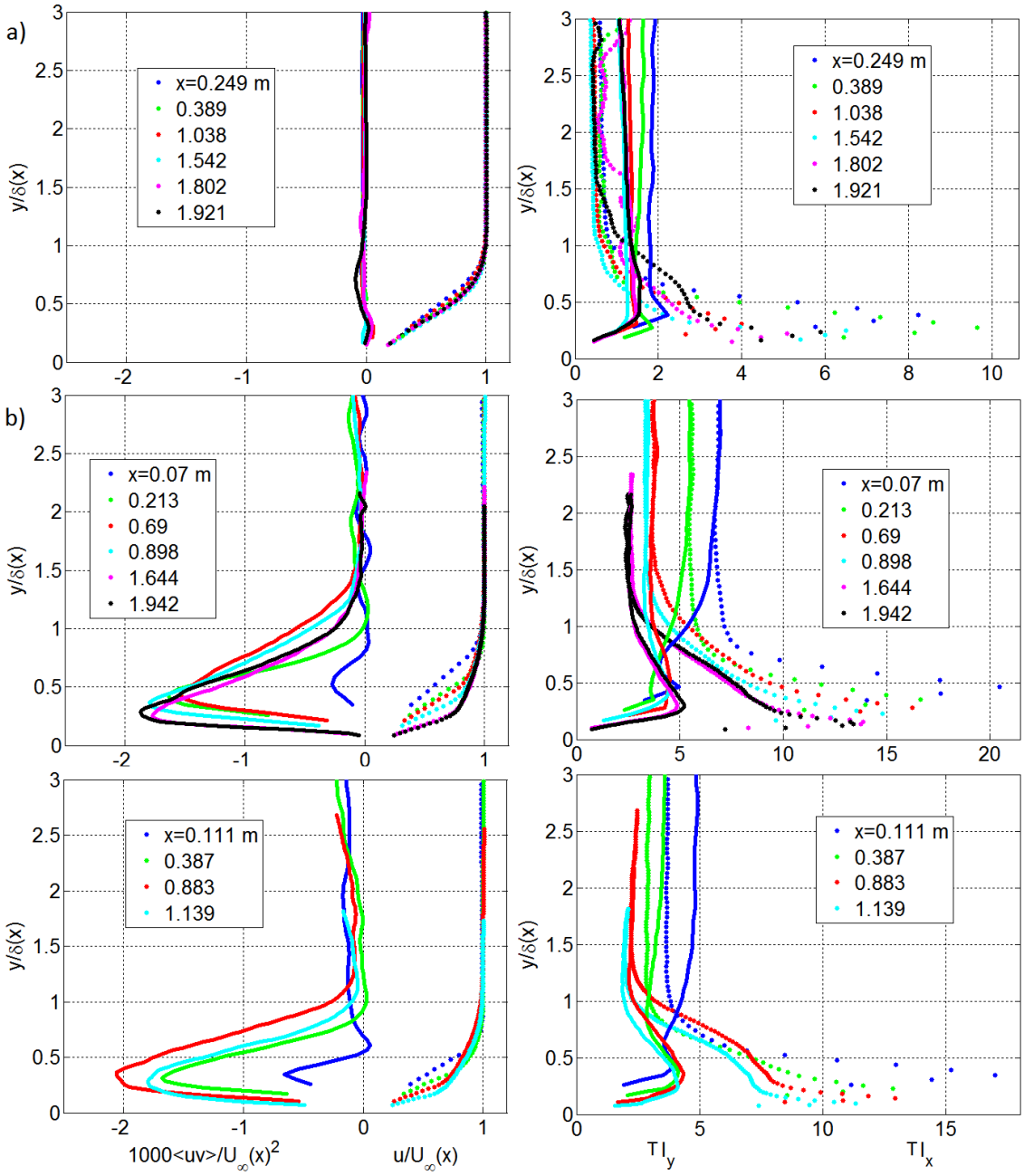

Figure 4.2: Normal to wall mean velocity profile and Reynolds shear stress x 1000 (left side), and normal to wall turbulence intensity profiles of x- and y-components of the flow (right side). Colors show progression down the length of the plate, x. (a) ZPG without TG. (b) ZPG with TG. (c) APG with TG.

Table 4.1: Numerical solution of the Blasius boundary layer, Equation 4.15

η	f'	η	f'
0	0	2.6	0.9306
0.2	0.09391	2.8	0.95288
0.4	0.18761	3	0.96905
0.6	0.28058	3.2	0.98037
0.8	0.37196	3.4	0.98797
1	0.46063	3.6	0.99289
1.2	0.54525	3.8	0.99594
1.4	0.62439	4	0.99777
1.6	0.6967	4.2	0.99882
1.8	0.76106	4.4	0.9994
2	0.81669	4.6	0.9997
2.2	0.8633	4.8	0.99986
2.4	0.90107	5	0.99994

where f is a function of η, and f' is U/U_∞ (not explicitly in the equation). The boundary conditions for the non-linear ODE are as follows

$$f'(0) = f(0) = 0 \qquad f'(\infty) = 1 \tag{4.16}$$

the solution to Equation 4.15 can be easily found with a numerical shooting method. As there are various ways to solve the non-linear ODE given in Equation 4.15, the present work results are shown in Table 4.1 for clarity.

By evaluating equation 4.14 at a given location within the middle window of the MIR test section, a comparison can be made to the solution found in Table 4.1. By choosing the middle window this allows for enough distance to remove any effects from the leading edge, and the laminar boundary layer has developed enough to have substantial amounts of data within the said boundary layer. This comparison can be seen in Figure 4.3. The comparison works so well as explained by White [66], that within laminar-boundary-layer flow there is no characteristic length, "L." Therefore, all laminar-boundary-layer profiles have the same dimensionless shape (i.e., Tbl. 4.1 holds for all locations x in a laminar boundary layer).

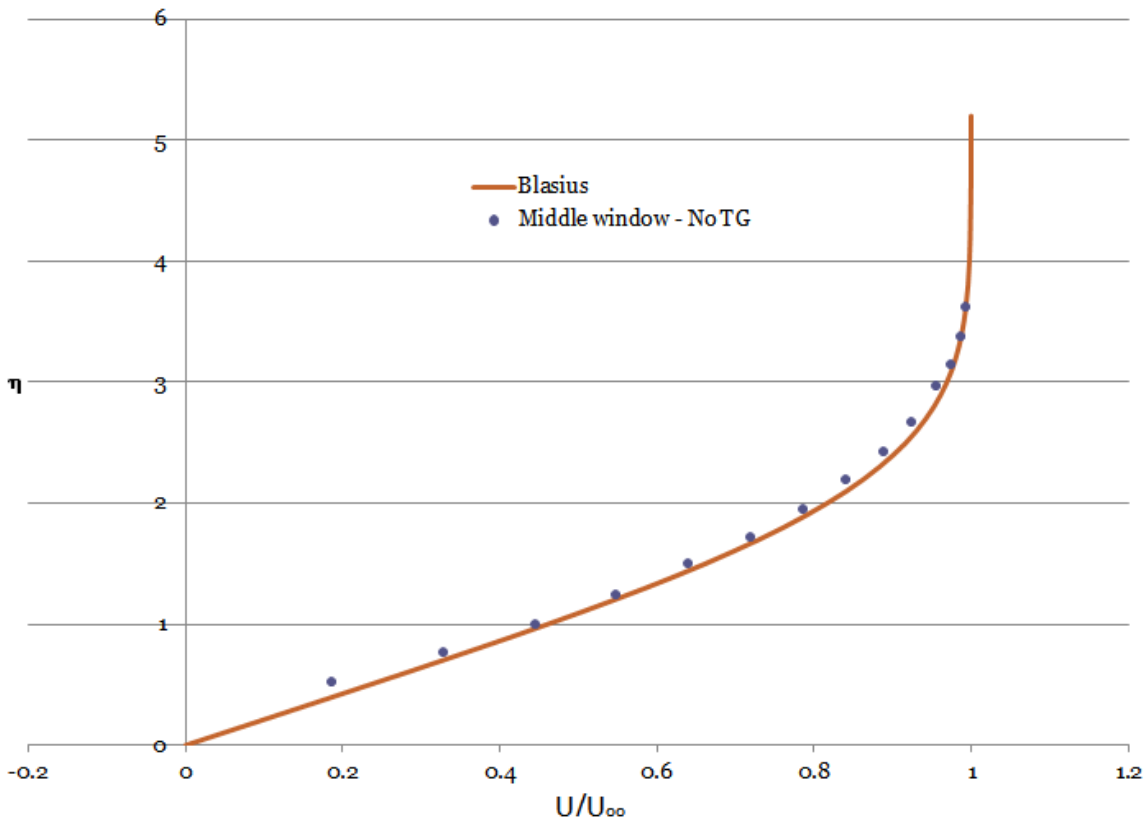

Figure 4.3: Laminar flow comparison of ZPG without TG (symbols) to the Blasius laminar-boundary-layer solution (line).

4.5 Skin Friction Coefficient

The skin friction coefficient defined from White [66] and utilizing the integral parameters that were defined above is

$$C_f = 2\left(\frac{d\theta}{dx} + (2+H)\frac{\theta}{d\theta}\frac{dU_\infty}{dx}\right) \tag{4.17}$$

with H as

$$H = \frac{\delta^*}{\theta} \tag{4.18}$$

and is called the shape factor of the boundary layer. H commonly follows a horizontal asymptote at ∼2.5 in a laminar boundary layer, and will slope downward towards another asymptote of ∼1.5 through the transitional region of the boundary layer

towards the fully developed turbulent boundary layer (see White [66]).

To measure the skin friction coefficient directly one must follow the following two equations

$$\tau_w = \mu \left. \frac{dU}{dy} \right|_w \tag{4.19}$$

and

$$C_f = \frac{\tau_w(x)}{\frac{1}{2}\rho U_\infty(x)^2} \tag{4.20}$$

where τ_w is the local shear stress of the fluid at the wall, U is the time averaged velocity, and μ is the dynamic viscosity of the fluid. In equation 4.20, ρ is the fluid density, and U_∞ is the local freestream velocity.

Johansson *et al.* [22] gives a rather straight forward method to finding the slope, dU/dy, of the shear stress at the wall. Data points ($\sim 15-20$) within $y^+ < 10$ (where y^+ is defined as yu_τ/ν) of the U velocity were measured within the MFOV, and a curve fit was applied to the data by using a Taylor-series expansion about U as a function of y

$$U = \left. \frac{\partial U}{\partial y} \right|_w (y - y_0) - \frac{U_\infty}{2\nu} \frac{dU_\infty}{dx} (y - y_0)^2 + \frac{1}{24} \left. \frac{\partial^4 U}{\partial y^4} \right|_w (y - y_0)^4 + O(y^5) \tag{4.21}$$

where subscript w means the measurement at the wall, and the leading coefficient is the slope of the velocity gradient at the wall. There is also an offset built into the equation to correct for the wall location. This offset is needed because the measurements of velocity are recorded on a regular grid, and (more than likely) the apparent image of the plate lies in between the grid nodes. The second term has an interesting coefficient that comes from $\left(\partial^2 U/\partial y^2\right)_w = \frac{1}{\mu}\frac{dP_\infty}{dx} = -\frac{U_\infty}{2\nu}\frac{dU_\infty}{dx}$, and concerning the third derivative it is known that $\left(\partial^3 U/\partial y^3\right)_w = 0$ making that specific term null. Further, the fourth order derivative is as shown, and all higher order terms are neglected.

By applying a numerical mask that removes erroneous data within the plate, and also any residual errors from the wall into the flow (around 2 grid nodes), and iterating

on the above curve fit (Eq. 4.21), the data had enough points below the $y^+ < 10$ criterion (as seen in Fig. 3.7). The iteration on Eq. 4.21 was computed within a while loop until the y^+ values had not changed from one iteration to the next below a cutoff of 10^{-3}, then the iteration is deemed sufficient and the velocity gradient at the wall was recorded. The change in y^+ values arouse considering that with every iteration a "better" velocity gradient at the wall ($\mathrm{dU/dy}|_w$) was observed (differing from the previous calculations), and the y^+ values would change slightly. In more detail, the consistent PIV/PTV grid of velocity vectors with known spatial dimensions would stay constant, and the improved velocity gradient at the wall changed with every iteration of the Eq. 4.21, thus changing y^+.

An example of the curve fit U vs. y using Eq. 4.21 can be seen in Figure 4.4. The data is taken from the APG dataset with an x location of x = 855 mm from the leading edge. The figure shows the traditional $y^+ = U^+$ curve (where U^+ is defined as U/u_τ, and $u_\tau = \sqrt{\tau_w/\rho}$) for the viscous sublayer as a dashed line, and the APG with TG measured data as circles, $\circ$. The Johannson curve (seen as a solid line in the same figure) fits near perfectly down the middle of the APG data, and around y^+ of 3 the dataset meets up with the viscous sublayer. This is consistent with observations made bt Walsh *et al.* [63].

Looking now at equation 4.20 for the skin friction coefficient, it is important to understand the characteristics of the coefficient in the laminar, transitional, and turbulent regimes of the flow over a flat plate. Theoretically, C_f comes down from positive infinity at the leading edge of the plate, then reaches a local minimum at the onset of transition, followed by a maximum where the turbulent boundary layer is formed. The local minimum of C_f at the onset of transition is at a different location along the plate based on several factors: FSTI, pressure gradient, inlet conditions, etc. Mayle [32], Abu-Ghamman and Shaw [1], and Dunham [10] have all addressed this transition location, and based it on a criterion they all call $Re_{\theta t}$, or in other words

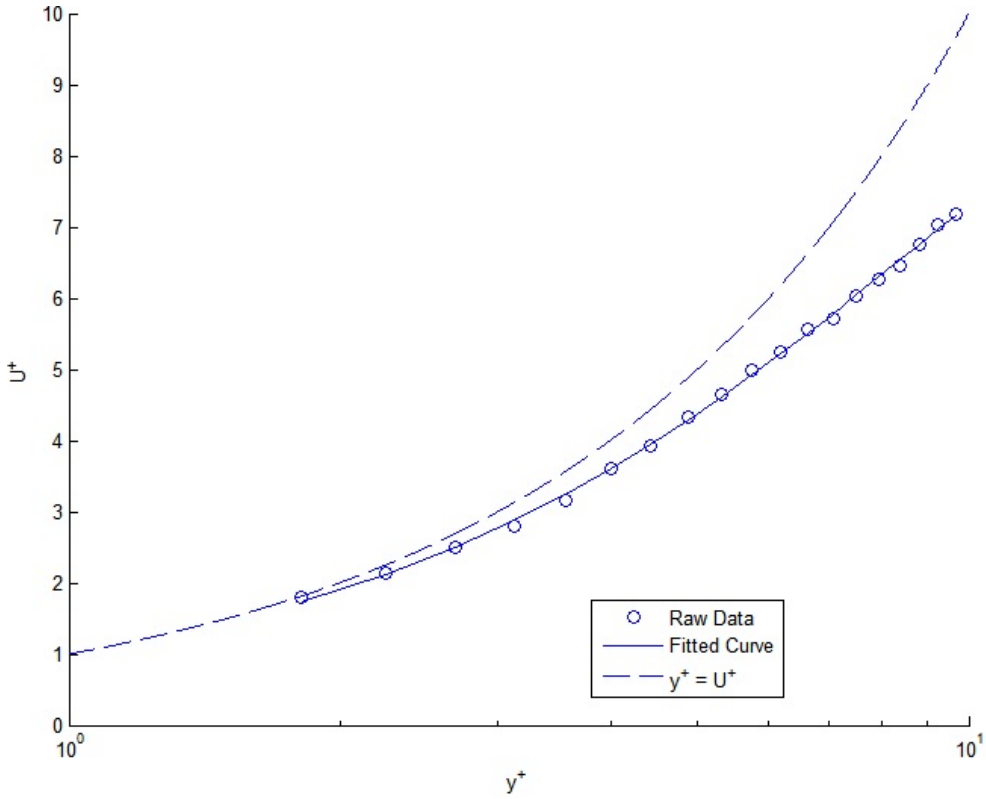

Figure 4.4: Curve fit using equation 4.21 to measure streamwise-normal velocity gradient at the wall. Showing U^+ vs. y^+ as the viscous sublayer. Data from APG with TG, and at x = 855 mm.

a critical Reynolds number based on momentum thickness. The three cited authors each have their own approach to the transition location and are repeated here

$$\text{Mayle [32]:} \qquad Re_{\theta t} = 400 FSTI_x^{-5/8} \tag{4.22}$$

$$\text{Abu-Ghamman and Shaw [1]:} \quad \begin{aligned} Re_{\theta t} &= 163 + e^{F(\lambda_\theta) - F(\lambda_\theta)\tau/6.91} \\ \lambda_\theta < 0 &: F(\lambda_\theta) = 6.91 + 12.75\lambda_\theta + 63.64\lambda_\theta^2 \\ \lambda_\theta > 0 &: F(\lambda_\theta) = 6.91 + 2.48\lambda_\theta - 12.27\lambda_\theta^2 \end{aligned} \tag{4.23}$$

$$\text{Dunham [10]:} \quad \begin{aligned} Re_{\theta t} =& (0.27 + 0.73 e^{-0.8\overline{FSTI_x}}) \cdot \\ & (550 + \frac{680}{1 + \overline{FSTI_x} - 21\lambda_\theta}) \end{aligned} \tag{4.24}$$

where $FSTI_x$ is defined in 4.8, and λ_θ is the pressure gradient coefficient. Note that

Dunham recommends the use of the average of the two FSTI measurements at the leading flow conditions (i.e., before the plate or just at the leading edge) and just above the onset of transition location. This is slightly misleading as the equation is trying to discover the onset of transition location in and of itself, but a best guess will suffice.

Table 4.2 shows the utilization of Eqs. 4.22 – 4.24 to predict the transition locations of the boundary layers for each flow configuration. The predictions for the ZPG w/out TG were drastically different from each other, as the low FSTI in this case is a poor indicator of transition. While on the other two flow conditions, the higher FSTI allows for a more realistic prediction of transition location. Note that the observed transition location for the APG w/ TG case is before the domain of the dataset which begins at $Re_\theta = 180$, and this is further clarified by the predictions made for that dataset ($Re_\theta = 168 - 174$).

In summary, transition for both ZPG with TG and APG with TG cases should transition early due to their high freestream turbulence intensity and/or adverse pressure gradient; while, in contrast, the ZPG without TG should transition much later due to the quite freestream and 'negligible' pressure gradient. The values of C_f and H are plotted together over the length of the plate in Fig. 4.5 for each flow configuration. This plot, and Tbl. 4.2, can be compared to better understand the location for transition to occur. In the ZPG without TG case (Fig. 4.5a), the transition *may* be seen towards the end of the plate; where transition is seen as a local minimum on the C_f curve. However, the shape factor does not appear to support the C_f curve, as it stays around the horizontal asymptote of 2 - 2.5. This is also consistent with the aforementioned predictions, as each prediction is outside (i.e., downstream) the domain of the dataset. In the ZPG with TG flow configuration the onset of transition is observed to be around $Re_{\theta t} = 163$. The shape factor, H, is also consistent with this observation as it comes downward from the expected laminar value, and transitions

Table 4.2: Comparison of predicted to observed transition locations – based on the critical momentum thickness Reynolds number, $Re_{\theta t}$ – for all three flow configurations.

Author	Equation	Experiment	ZPG w/out TG	ZPG w/ TG	APG w/ TG
Mayle [32]	$Re_{\theta t} = 400TI^{-5/8}$	Others	480	110	168
Abu-Ghamman and Shaw [1]	$Re_{\theta t} = 163 + e^{F(\lambda_\theta) - F(\lambda_\theta)\tau/6.91}$ $\lambda_\theta < 0 : F(\lambda_\theta) = 6.91 + 12.75\lambda_\theta + 63.64\lambda_\theta^2$ $\lambda_\theta > 0 : F(\lambda_\theta) = 6.91 + 2.48\lambda_\theta - 12.27\lambda_\theta^2$	Open-circuit wind tunnel	650	163	172
Dunham [10]	$Re_{\theta t} = (0.27 + 0.73e^{-0.8\overline{FSTI_x}}) \cdot (550 + \frac{680}{1 + \overline{FSTI_x} - 21\lambda_\theta})$	Others	418	150	174
Observed Transistions	–	–	–	160	< 180

into the turbulent region. As noted above the local freestream velocity is utilized to calculate the skin friction coefficient. Therefore, as the tunnel has a slight favorable pressure gradient from boundary layers forming on all sides, the skin friction coefficient is lower in magnitude (vs. the expected trend) within the turbulent boundary layer from the slight increase in freestream velocity – found in the denominator of Eq. 4.20. The APG with TG flow condition has an onset of transition that is assumed to have already occurred before the domain of the data (with more on this specific assumption below). In Fig. 4.5c, the shape factor, H, for this flow configuration follows the traditional trend of $\sim$1.5 for the fully turbulent regime – with the transition region coming downward towards that value. This is also consistent with the predictions in Tbl. 4.2.

4.5.1 Note on Particles Resting on Plate Surface

In a related topic, and as mentioned above, the particles that rested on the plate surface were magnitudes smaller than the lowest detactable measurement of the flow. The average particle diameter was $12x10^{-6}$ m, and the smallest detectable measurement was on the order of 10^{-4} m. Further, the sublayer, as an order of magnitude, was approximately on that same scale of 10^{-4}. This shows that the viscous effects of the fluid dominate the effects from any singular particle resting on the plate surface, and does not lead to any form of a "trip" from within the viscous sublayer. In other words, the main effects of transitional behavior comes from the high freestream turbulence, and not from the particles resting on the flat plate.

4.6 Integral Length Scale

The turbulent eddies throughout the flow are of an entire spectrum in size from the largest eddies, down to the Kolmogorov length scale, and on to dissipation into heat. In order to capture the average large eddy size an algorithm was made, and

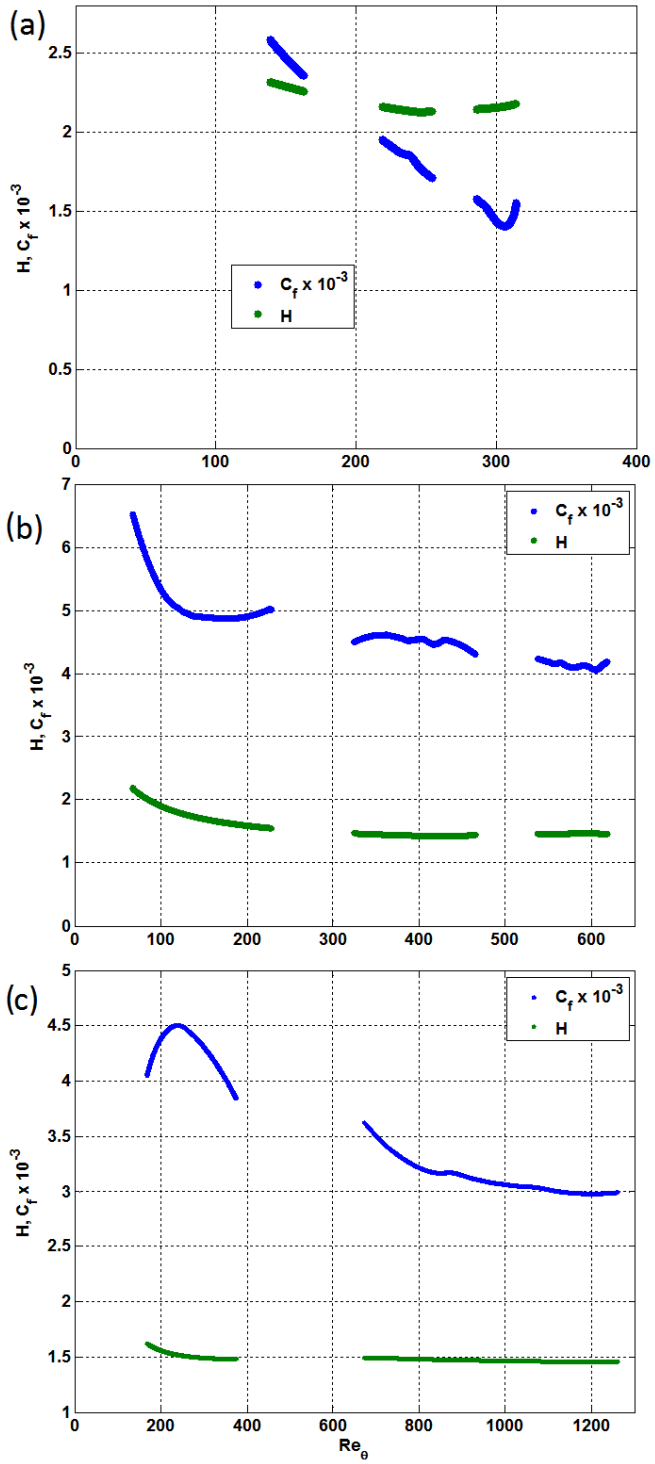

Figure 4.5: Skin friction coefficient and shape factor (H = δ^*/θ) for the three cases shown. (a) ZPG without TG. (b) ZPG with TG. (c) APG with TG.

utilized on the free stream velocity in both the x and y directions. The values were found using

$$L = \int_0^\infty f(r)dr \tag{4.25}$$

where f(r) is

$$f(r) = \frac{\overline{u'(x)u'(x+r)}}{\overline{u'(x)^2}} \tag{4.26}$$

where f(r) is streamwise measurements of velocity fluctuations that are separated horizontally by a vector, r. The upper limit of infinty was dropped from the integral of Eq. 4.25, and was replaced by an upper limit of approximately 6". This was reasonable as the turbulent eddies were assumed to be around 1" to 2", and a simple order of magnitude study of the area under the correlation curve from Eqs. 4.25 and 4.26 is a triangle with height 1 and base 6" – which gives a 3" length. The 1" – 2" assumption comes from the conclusions made by Roach [44] that eddy length scale is on the order of the mesh diameter, M – which in this case is 1" – and grows (in a ZPG) at a rate of $\sqrt{x}$ downstream of the grid. This gives a correlation curve found in Figure 4.6, where the area under the curve is the total integral length scale of the turbulent eddies in the freestream. The curves were compared to Comte-Bellot and Corrsin [9]. It was found that the turbulent eddies in the freestream at or very near the transitional region of the boundary layer for the ZPG with TG case were ∼0.91" and for the APG with TG were ∼0.63".

4.7 Total Spatial Correlation

Nolan and Walsh [39] utilized the Pearson Correlation, R, as a total spatial correlation. It follows suit with the integral length scale presented in Section 4.6, but herein the correlation location was evaluated with all space in all directions. The outcome is presented (in landscape) for the ZPG with TG and APG with TG cases in

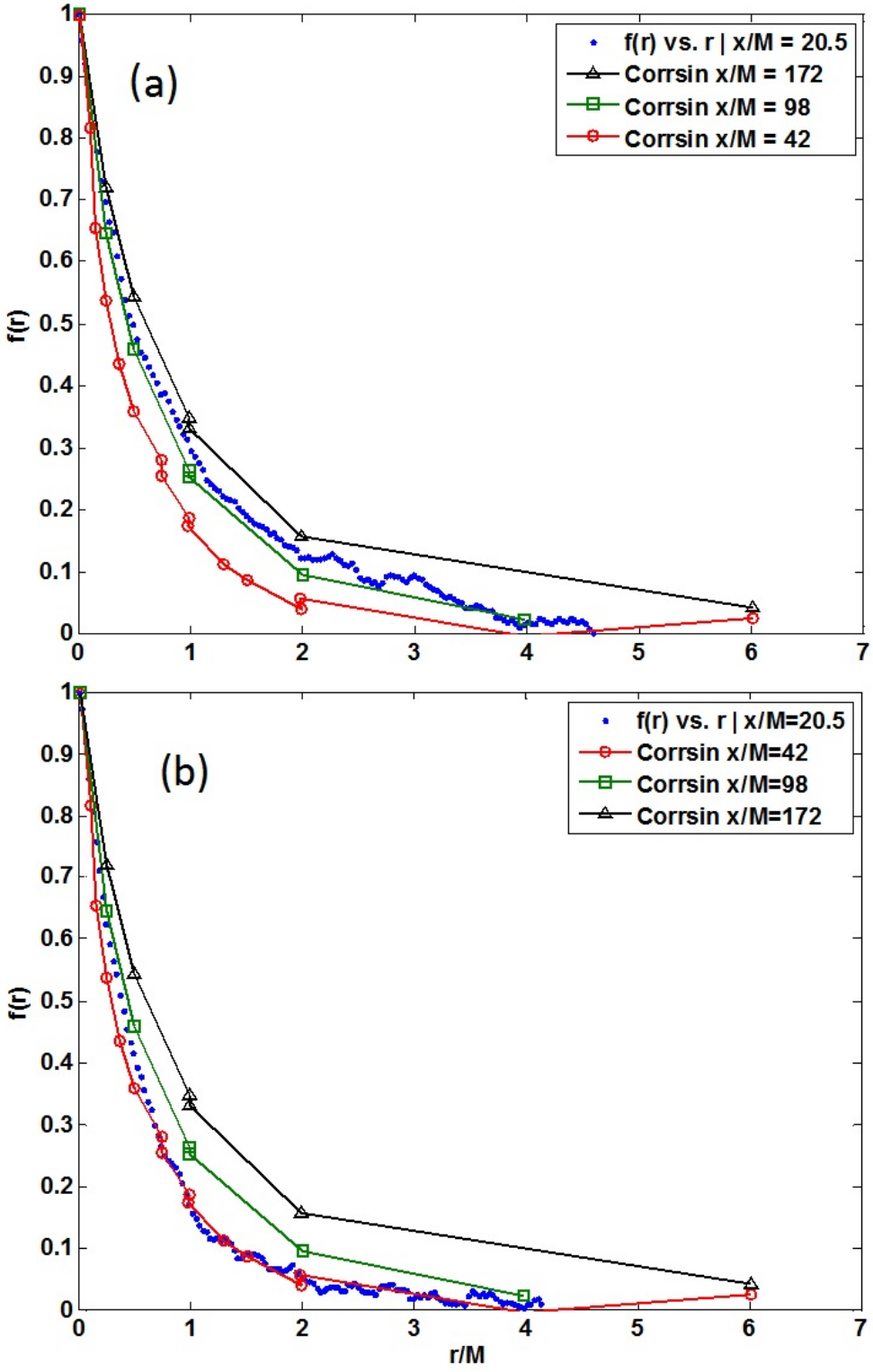

Figure 4.6: Spatial correlation curves. (a) ZPG with TG and (b) APG with TG. ZPG without TG not shown.

Figure 4.7 and Figure 4.8, respectively. Where column-wise representation is a given x location down the length of the plate, and row-wise representation are different y/δ locations from 0.2 - 1.4, with a 0.2 increment. The dashed line is the boundary layer thickness at each location. Each individual image starts at total correlation, $R_{uu} = 1$ (red) and moves outward until the cutoff criterion of $R_{uu} = 0.3$ (blue).

These correlation maps show that at higher free stream turbulence levels, the free stream turbulence effects the boundary layer up to the point where the boundary layer becomes turbulent itself, independent of the freestream. At this point, the correlation of freestream turbulence and boundary layer turbulence are separated, as the boundary layer is now producing unique turbulent eddies to the freestream. Where, also, very near the wall the lift-up angle can be observed for all post transitional locations [39].

As stated earlier, the APG w/ TG flow configuration developed a boundary layer that was too large for the optics used in the current work (see Fig. 3.6). The "blank" boxes in Figure 4.8, show where the freestream information was not recorded.

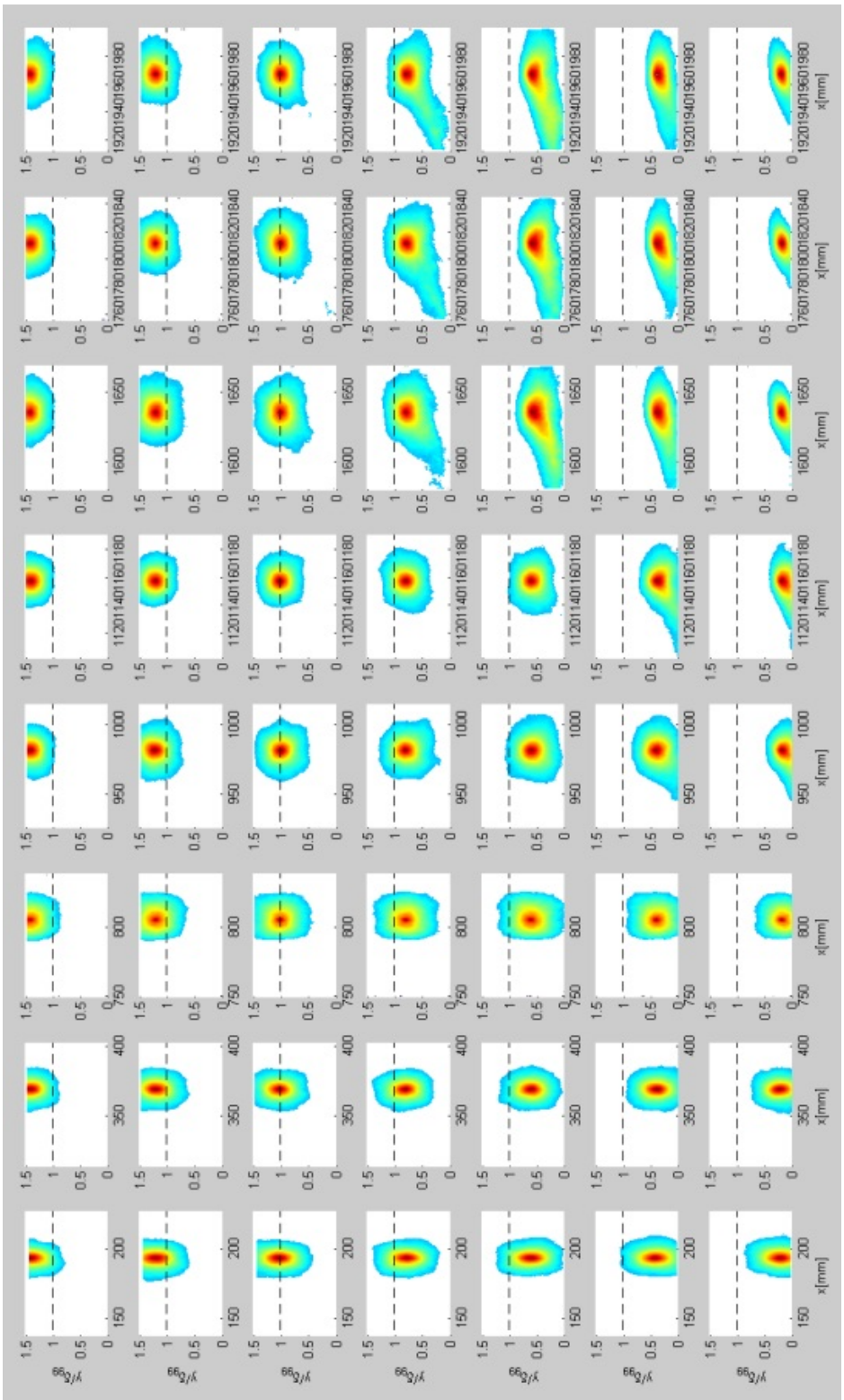

Figure 4.7: ZPG with TG total spatial correlation of u'. Note: Image is in landscape.

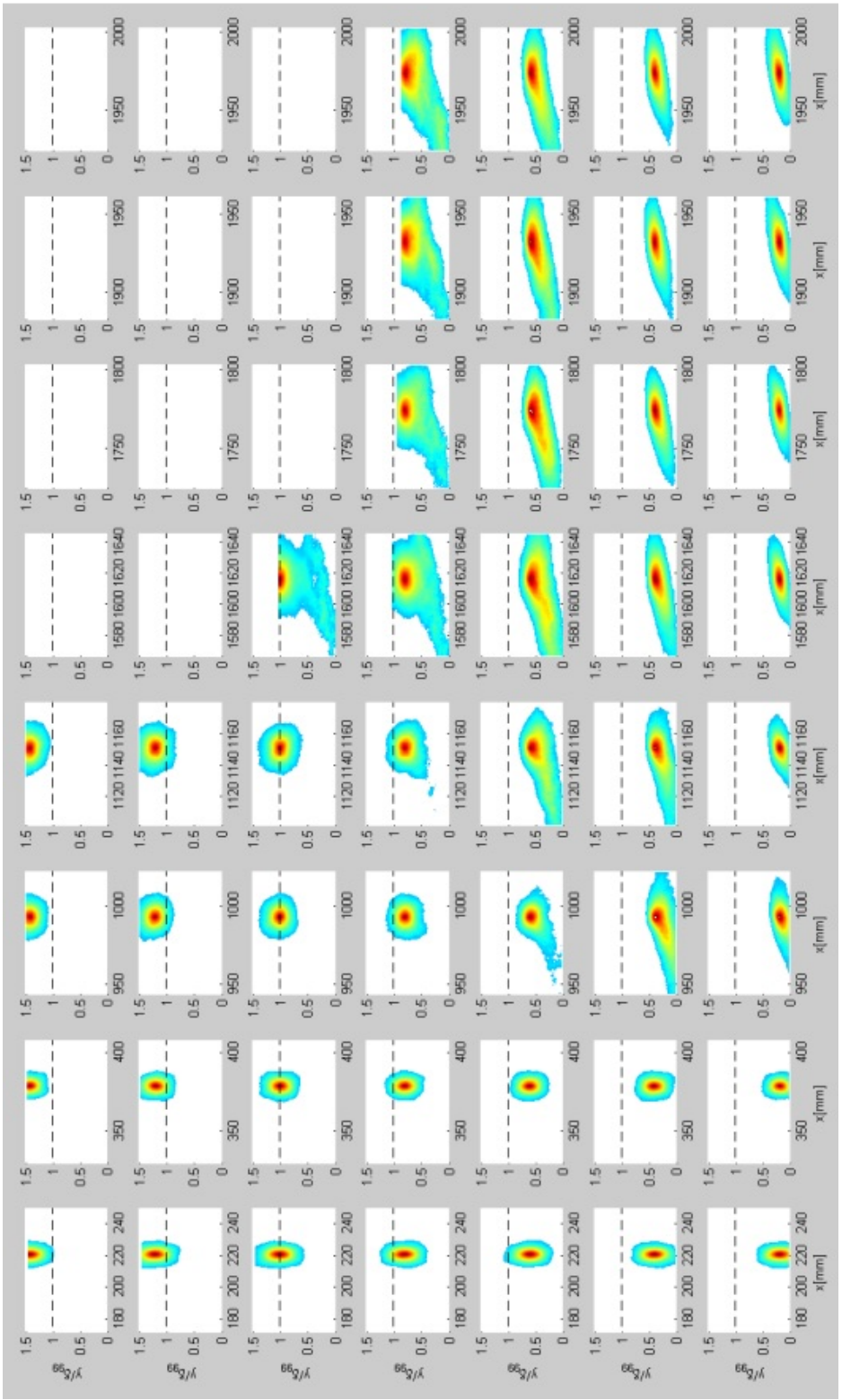

Figure 4.8: APG with TG total spatial correlation of u'. Note: Image is in landscape.

Chapter 5

Correction to Wall Shear Stress Using Particle Distribution Centroid

In the close proximity to the wall, in the high shear region of the flow, the seeding particles become sparse or spread out across the viscous sublayer ($y^+ <= 10$, and beyond). This causes the PIV velocity reading in the area to be biased upwards, as the resulting velocity within an interrogation window (IW) has only detected the higher velocity which exists in the section of the IW that is further from the wall. In order to correct for this biased error in near wall measurements it was proposed to look at the particle distribution centroid of the IW as the "correct" measurement location, instead of the industry standard of the geometric center of the IW. The purpose of this method is to model the particle distribution within an IW by looking strictly at the intensity of the IW signal, and reporting the intensity centroid as the "true" velocity measurement location.

The biased dispersion of seeding particles within an IW can come from multiple sources. These can either act independently or in unison, amplifying the problem. A small normal to the plate velocity component, v, pushes the seeding particles away from the plate. Citing the conservation of mass, there is also the growth of the boundary layer where seeding present at the beginning of the plate (small developing boundary layer) is now spread out over a much larger boundary layer downstream. The turbulent eddies in the freestream do not penetrate the viscous shear layer deep inside the boundary layer as much as they did near the leading edge of the plate. This means any momentum feeding eddies that could provide the boundary layer with more seeding particles from the freestream cannot penetrate the viscous sublayer [41]. Another mode of scarcity of seeding particles in the boundary layer is from a heated plate, where the buoyancy effect and the expansion of the heated fluid pushes the

seeding particles away from the solid boundary [19][18]. The later is presumably the most prevalent, and will be discussed below.

5.1 Methods Used to Find the Particle Dispersion Centroid

Similar to that of Theunissen *et al.* [53] and Usera *et al.* [55], an algorithm was written to capture the intensity centroid of each IW in PIV. The main difference from that proposed by Theunissen is that IWs were only analyzed *above* the wall interface, and had only the effects from biased particle dispersion. In other words, the present work looked specifically at flow measurements when the seeding was (on average) biased away from a physical interface. The algorithm allowed for the biased error, from the above mentioned sources (if present), in velocity vector location to be corrected, and brought the velocity gradient at the wall into its correct location and profile. Any random error from the intensity centroid instantaneous fluctuations – if a concern – is beyond the scope of this work.

The intensity centroid was found using the following

$$C_x(m,n) = \frac{\sum_{k=1}^{M}\sum_{l=1}^{N}[x(k,l)f(k+m,l+n)]}{\sum_{k=1}^{M}\sum_{l=1}^{N}[f(k+m,l+n)]} \tag{5.1}$$

$$C_y(m,n) = \frac{\sum_{k=1}^{M}\sum_{l=1}^{N}[y(k,l)f(k+m,l+n)]}{\sum_{k=1}^{M}\sum_{l=1}^{N}[f(k+m,l+n)]} \tag{5.2}$$

where C_x and C_y are the image intensity centroid of the IW in the x and y directions, respectively. The f matrix is the image signal, and the x and y matrices are the pixel locations for moment leverage to each pixel in the IW. The algorithm asked for certain user inputs that were used in PIV: IW size and overlap. This made sure the grid size matched between PIV and the search for IW intensity centroids. An example of the intensity centroid location can be seen in Figure 5.1. The illustration

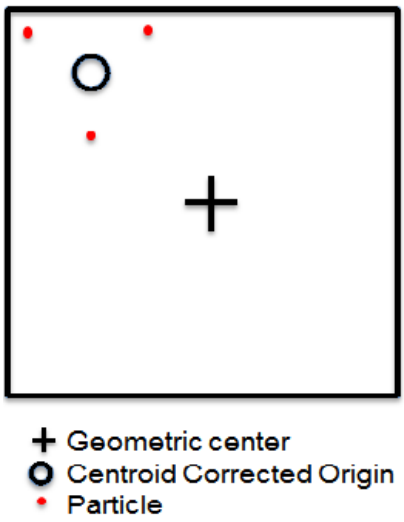

Figure 5.1: Example illustration of intensity centroid location versus geometric center of an IW.

in Figure 5.1 shows the geometric center of the IW (where the reported vector from PIV would be recorded) as a cross, +, the synthetic particles as dots, ·, and the new intensity centroid of the particles as a circle, ∘. The location of the intensity centroid would be recorded and repeated for all locations in an image, and then again through the rest of the images in the set (e.g. 4,000 for the MIR datasets). The ensemble average centroid location is then computed with the purpose of correcting the previously ascertained PIV vector output of IW geometric centers.

To improve the output of equations 5.1 and 5.2, one of the challenges was to remove background noise (e.g. reflections, current in the camera chip, etc.) from the true signal of the particles. An algorithm was used to quiet down or completely remove any noise, in order to specifically look at true signal from the particles in the flow. The intensity centroid search windows (identical in size and location to the IWs used in PIV) were scaled up by 2 or 3 times the corresponding PIV IW size. This allowed for even better statistics and improved signal to noise ratio. A standard deviation (using 95% confidence) of the signal from the average signal was computed from this scaled search window. The signal floor was then removed below -3σ within

that IW. This process then swept across each location within the image; finding the intensity centroid within each IW to match the exact grid size from the ascertained output from PIV.

5.2 Results From the Particle Dispersion Centroid

Two cases have been analyzed to demonstrate the need for correction to the biased error in wall bounded flow. They are the aforementioned ZPG without TG case, and a dataset from a vertical heated plate with forced convection flow provided to the author by Harris *et al.* [19]. An example of the particle dispersion from the heated plate dataset (discussed below in 5.2.3) can be seen in Figure 5.2. The bright strip of light near the left of the figure is the wall interface, and the seeding used in PIV can be seen in the bulk of the image. Flow is going from bottom to the top. The seeding very near the wall can be seen thinning out, causing rise to be analyzed by the intensity centroid method.

5.2.1 ZPG without TG Dataset From the Matched Index of Refraction Flow Facility

The biased dispersion of particles near the plate was not pronounced enough within the ZPG without TG dataset. However, the laminar flow of the ZPG without TG dataset, could be compared with the Blasius solution (a laminar analytical solution for wall bounded flow). This was ideal to see how much the centroid correction method was needed to correct the seeding disparity at the wall. Therefore, a strip of the image was masked out numerically with zeros just above the horizontal flat plate to imitate the seeding disparity found elsewhere. This is seen as a red rectangle in Fig. 5.3 where the flat plate is towards the bottom of the image (seen as a horizontal bright strip of intensity just below the mask), and the flow itself takes up the bulk of the image – flowing from right to left. The mask was a step function of zeros at

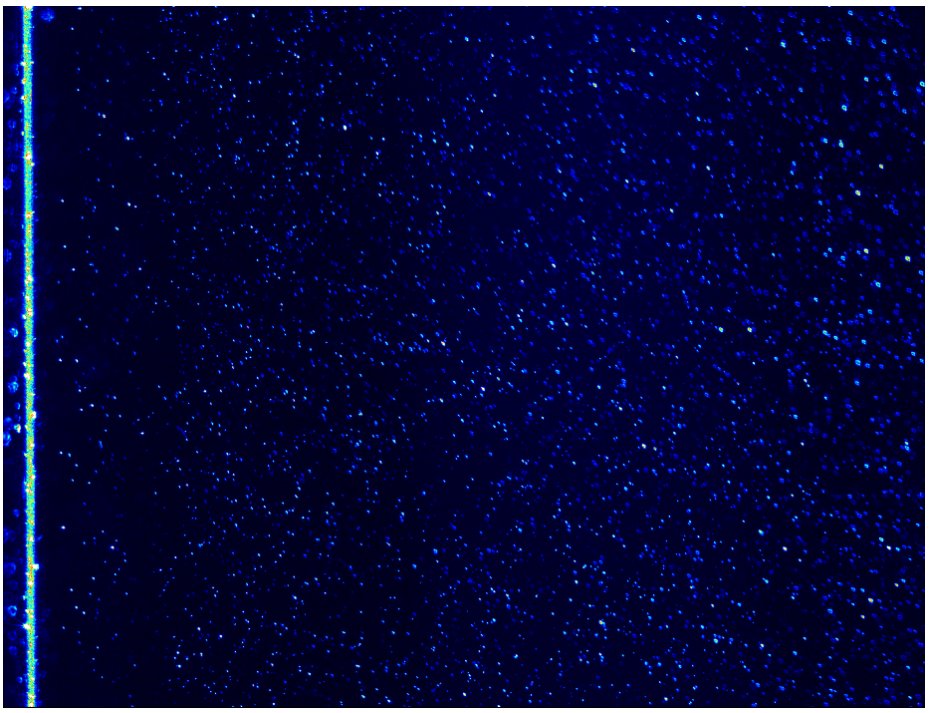

Figure 5.2: An example image frame of particles being moved from the wall boundary (bright strip of light near the left side of the figure).

32 pixels in the normal direction to match the PIV IW size, and spanned the entire length of the image.

The results from the laminar ZPG without TG dataset was compared to the analytical solution of the self similar Blasius profile and to a DNS solution of a laminar boundary layer provided by Owen *et al.* [42]. In Fig. 5.4 – with the axes in Blasius' similarity variables – the "as-is" output from the PIV software is reported as filled circles, •, while the centroid corrected data is reported as hollow circles, ∘. This figure shows that far enough away from the plate the two outputs coincide with one another, as the hollow circles are at the same location as the filled circles. Conversely, as the PIV IW approaches the wall in the normal direction the velocity reading is biased upward (i.e., faster than should be reported), and diverges from the "true" solution as the self-similar Blasius solution, shown as 'x' in Fig. 5.4. The DNS laminar boundary layer solution is also shown as a solid line, —, and further solidifies

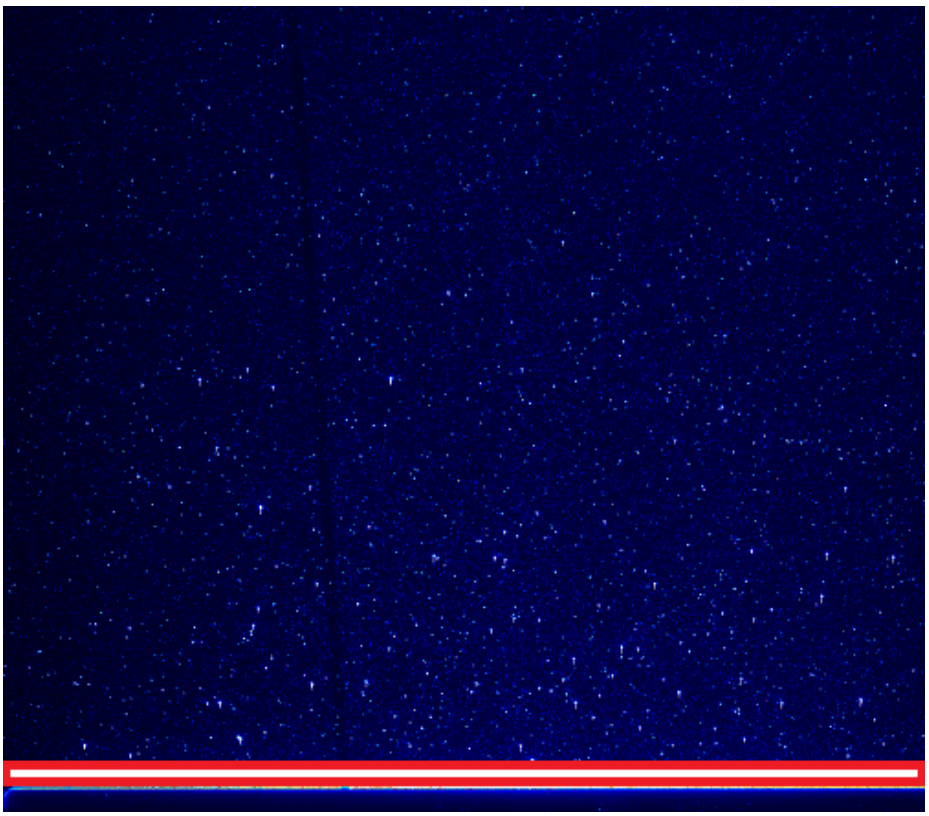

Figure 5.3: The numerical mask of zeros (red rectangle) applied to the flow as a step function – very near the wall – in order to amplify the seeding disparity in a high shear region.

the need to improve the velocity measurement locations in the close proximity to the wall. At this same proximity to the wall, the centroid correction method reports the measurements at their "true" location, and aligns the reported location of the velocity measurement with the Blasius and DNS solution.

In terms of error from the DNS, the velocity measurement location (reliable data point closest to the wall) had an error of 27.9% using the geometric centers of the IW (traditional PIV), down to an error of 1.8% for the centroid corrected method. Further, the error in the velocity gradient at the wall (i.e., dU/dy – which is proportional to the wall shear stress), when compared to the velocity gradient at the wall from the DNS curve, went from 53.5% error for the reported geometric centers of the IWs, all the way down to 8.7% error for the centroid correction method. The importance

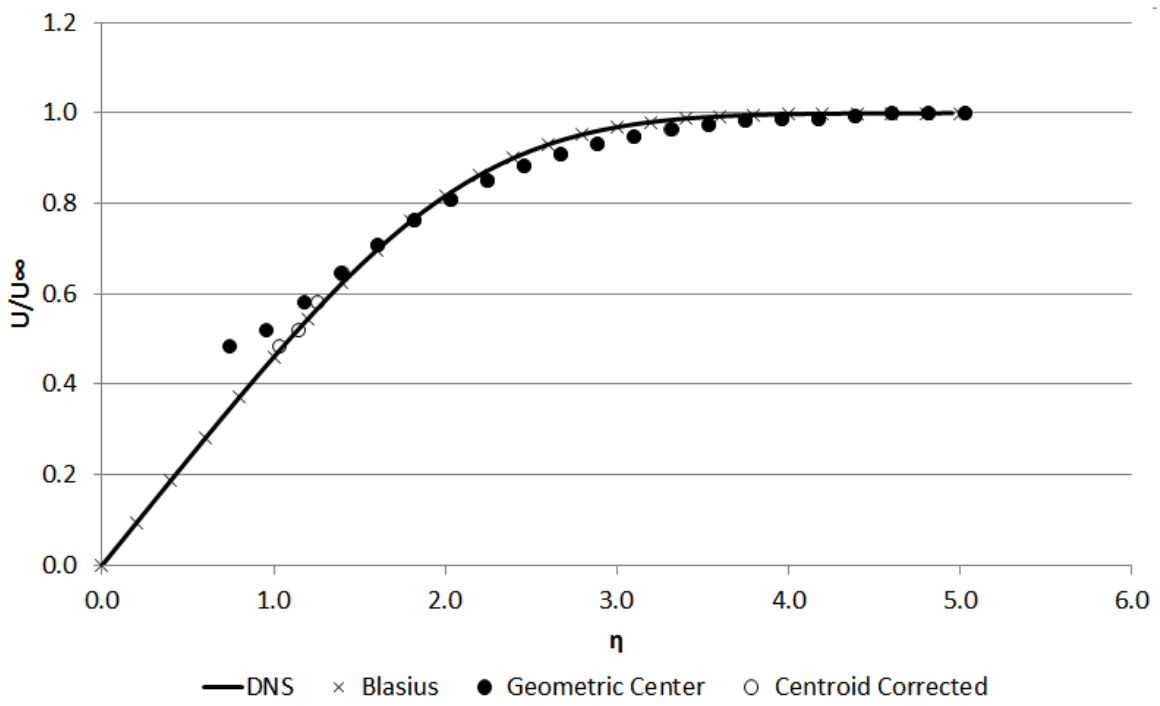

Figure 5.4: Biased correction of measurements within close proximity to a wall.

of the $dU/dy\big|_w$ measurement (and the difficulties of obtaining the measurement) will be discussed below.

5.2.2 APG with TG from the MIR

The need for the intensity centroid correction method was also seen within the transistional boundary layer of the APG with TG flow configuration. The flow configuration was utilized to study conditions inside the transitional boundary layer; coincidently the seeding very near the plate was seen to have a biased dispersion away from the plate inside this transitional boundary layer. This allowed for the images to be evaluated as-is, and did not require any additional modifications to the image set as was seen in the ZPG without TG flow configuration. It is assumed the biased dispersion of particles came from the local seeder discussed previously held just at the leading edge of the plate.

After running both PIV and the centroid correction code on the image set, the

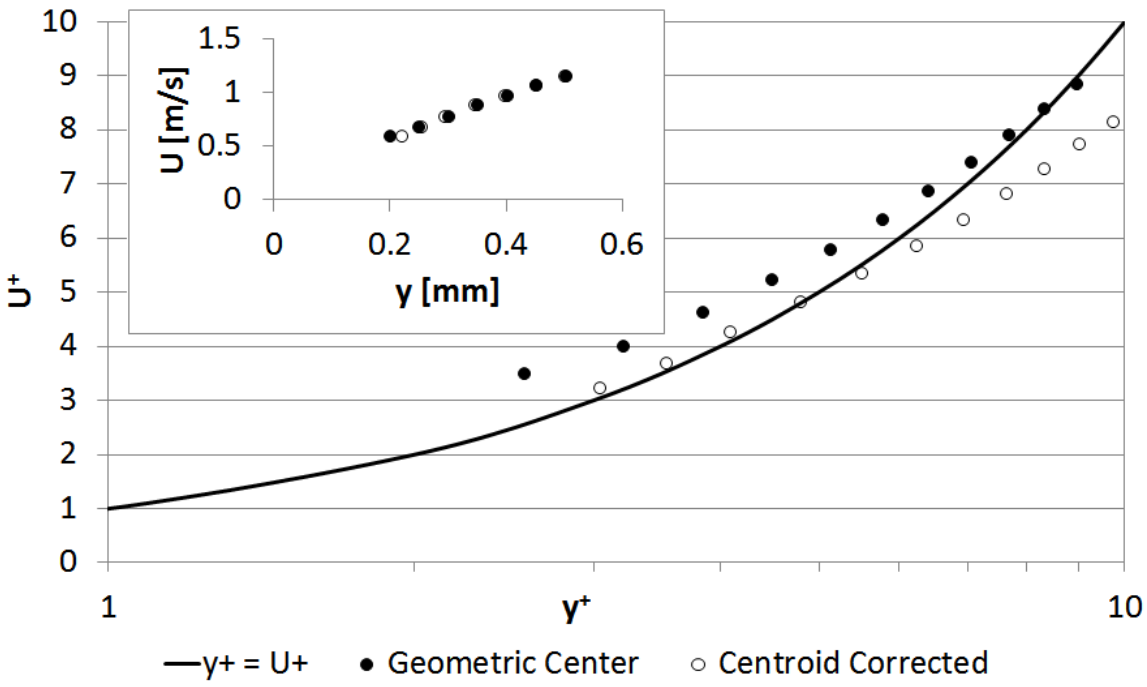

Figure 5.5: Biased particle dispersion correction of measurements within close proximity to a wall of the APG with TG dataset.

correction to velocity locations can be seen in Fig. 5.5 – where the symbols are similar to that in Fig. 5.4. The corrected locations of the velocity measurements can be seen in the inset where, for example, the velocity at approximately y = 0.2 mm is seen to be adjusted further away from the wall (i.e. y = 0 mm). These streamwise measuremenst in the wall-normal direction, in turn, directly effect the measurement of $dU/dy\big|_w$ and the wall coordinates that relate to that measurement. A significant improvement can be seen to the y^+ vs. U^+ data points on the semi-log plot. The centroid corrected viscous sublayer locations of the data points lie on top of the $y^+ = U^+$ relationship, and diverge away from the viscous sublayer around $y^+ = 5$.

The improvement to the velocity measurement location located at the first reasonable velocity measurement away from the wall (0.2 mm in the inset of Fig. 5.5; no flat plate information in the IW) was seen to be 9.5%. The improvement to the velocity gradient at the wall, $dU/dy\big|_w$, was 17.6% better than the as-is output of PIV.

5.2.3 Vertical Heated Plate With Forced Convection

To further verify the centroid correction method, a dataset by Harris *et al.* [19] was provided to the authors, because the biased particle dispersion was seen in the dataset – prevalent enough to avoid any modifications to the images. A detailed description of the experimental setup of this dataset can be found in [18].

Figure 5.2 shows the vertical heated plate on the left side of the figure as a bright band of light. The flow is going from bottom to top. The particles just to the right of the plate interface are thinned out enough to see the particle disparity with this single image. On average, the particles are in fact towards the right side of the IWs in this region. The same PIV processing, as in Tbl. 3.2, was performed on this image set, followed by the centroid correction method. After which the correction is made to the PIV output of velocity vector locations. The correction changes the velocity gradient at the wall – in this case $dV/dx\big|_w$ – which in turn effects the wall coordinates, x^+ and V^+.

In contrast to the ZPG without TG dataset shown above, there was no analytical solution to compare to for the heated-plate, forced-convection flow. It was decided to look to the very thin viscous sublayer location where only the viscous effects of the fluid dominate. The impact of the centroid correction method on the viscous sublayer – in wall coordinates – is clearly seen in Fig. 5.6. The figure shows an inset with x vs. V for both the geometric center and the centroid corrected locations. The velocity gradient at the wall (i.e., $\mathrm{dV/dx}\big|_w$) obtained from the velocity profile in the inset of Fig. 5.6 was then directly used to calculate the wall coordinates, x^+ vs. V^+ – shown in the main portion of the figure. The solid line in the figure is the traditional viscous sublayer curve where only the viscous effects of the fluid are dominate, and the dimensionless wall distance is equal to the dimensionless fluid velocity (i.e., in this case $x^+ = V^+$). Comparing the original wall coordinates with the corrected, the figure shows an excellent improvement to the data where the centroid corrected curve

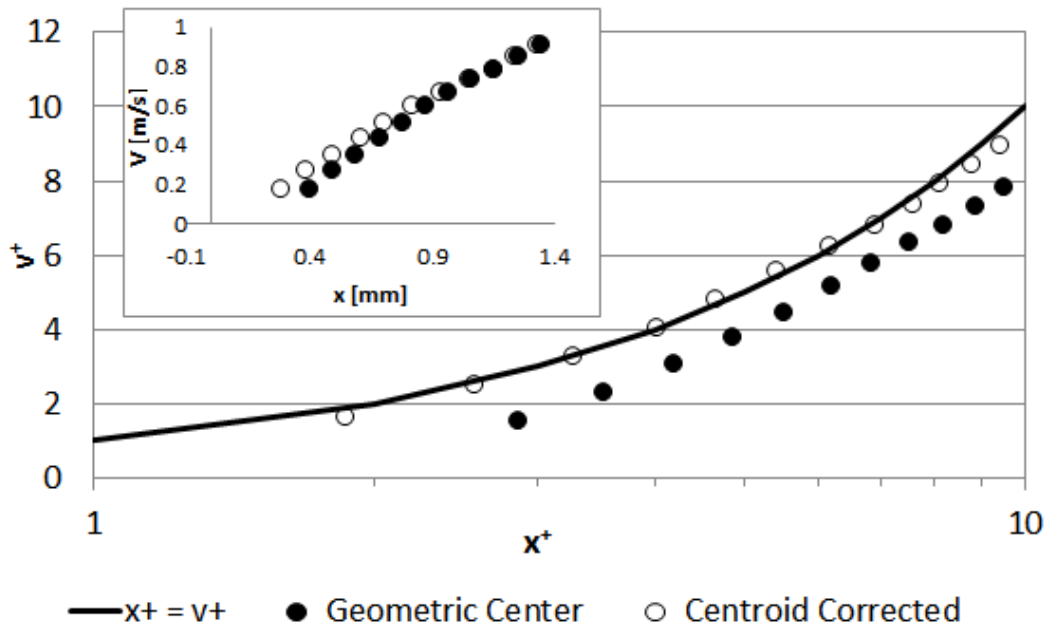

Figure 5.6: An example of the type of correction expected from removing the biased error in velocity measurement recorded location.

is basically on top of the $x^+ = V^+$ viscous sublayer curve.

Using the centroid corrected dataset as the 'correct' location of the velocity measurements, and observing the data point closest to the wall, there was a 41.9% improvement to the velocity measurement location from geometric centers to centroid corrected. Similarly, the velocity gradient at the wall was improved by 16.2% when the centroid correction method was utilized.

5.3 Discussion on the Need For and Application of the Particle Dispersion Correction

Measuring the velocity gradient at the wall with PIV is highly dependent on the optics used in each experiment. Two quick examples of how the velocity gradient at the wall can be elusive are either: 1) the magnification is too high and the seeding density is low, or 2) the magnification is too low and therefore velocity vector resolution is low, as well. Obtaining an accurate velocity gradient at the wall is important,

as it directly applies to various flow parameters that describe and/or model the flow. These parameters are (to name a few) the shear stress at the wall, τ_w, the friction velocity, u_τ, and the dimensionless wall coordinates, y^+ and U^+. Furthermore, wall shear stress is known to be an important parameter in several applications – including vascular flows, bedload sediment transport, and the skin friction component of the drag force. It is recommended by the author that one of the following two options be used to accurately obtain the velocity gradient at the wall.

Spalding [50] has shown a y^+ vs. U^+ curve fit that not only matches the no-slip condition at the wall, but also fits data well into the overlap region of the wall bounded flow. The equation is repeated here for simplicity

$$y^+ = U^+ e^{-\kappa C}\left[e^{\kappa U^+} - 1 - \kappa U^+ - \frac{(\kappa U^+)^2}{2} - \frac{(\kappa U^+)^2}{6}\right] \tag{5.3}$$

with $\kappa = 0.41$ and C = 5. Notice this equation is y^+ as a function of U^+, and once the data is fitted to the curve, the velocity gradient can be back calculated out of the equation. This method is more difficult to apply as an initial velocity gradient at the wall is "guessed", followed by an iteration of calculations until some convergence is met on the velocity gradient at the wall.

Johannson *et al.* [22] had a similar idea to curve fit the velocity data within $y^+ < 10$. By conducting a Taylor series expansion around U, they showed that the data can be fitted by

$$\begin{aligned} U =& \left.\frac{\partial U}{\partial y}\right|_w (y - y_0) - \frac{U_\infty}{2\nu}\frac{dU_\infty}{dx}(y - y_0)^2 \\ &+ \frac{1}{24}\left.\frac{\partial^4 U}{\partial y^4}\right|_w (y - y_0)^4 + O(y^5) \end{aligned} \tag{5.4}$$

where the coefficient to the first term is the velocity gradient at the wall. The second

order coefficient is equivalent to

$$\left.\frac{\partial^2 U}{\partial y^2}\right|_w = \frac{1}{\mu}\frac{dP_\infty}{dx} = -\frac{U_\infty}{\nu}\frac{dU_\infty}{dx},$$

the third order coefficient at the wall is equal to zero, the fourth order coefficient is as shown, and higher order terms are neglected. This method is, in the author's opinion, more straightforward when compared to Spalding's method, as the Johannson curve fit obtains the velocity gradient at the wall directly. The Johannson curve fit was used to calculate the velocity gradient at the wall for both aforementioned datasets.

It is recommended either Eq. 5.3 or 5.4 be utilized to obtain the velocity gradient at the wall. In this way the measurements from the wall up to the measurements in the overlap layer can all be useful. In any case, the correction from the centroid correction method needs to be utilized in the near wall region of the flow in order to correct for the biased error in velocity measurements.

Chapter 6

Pointwise Entropy Generation Rate

The flow configurations discussed above were utilized to fundamentally understand the pointwise distribution of entropy generation rates in transitional and pre-transitional flow. More importantly, the introduction of high freestream turbulence intensities and streamwise pressure gradients were used to "bypass" the Tollmein-Schlichting waves that occur in quiet boundary-layer-transition processes. Integral calculations of entropy generation rate per unit area were performed using Eq. 2.5; as well as pointwise entropy generation measurements using Eq. 2.3. The former integrates over the normal to the plate direction (i.e., y-direction) at each streamwise location, and produces a streamwise profile of the entropy generation rate. The latter is a makeup of the viscous and turbulent contributions at a single location in space. Further, Eq. 2.3 can be integrated in physical space, and compared to Eq. 2.5, S'', through the means of the dissipation coefficient, C_d (Eq. 2.7).

6.1 Integral Entropy Generation Rate

The integration of each term of Eq. 2.5 was calculated by means of the trapezoidal rule in physical dimensions, and then converted into wall coordinates by means of

$$S''^{+} = \frac{TS''}{\rho u_\tau^3}. \tag{6.1}$$

where S'' is explicitly

$$
\begin{aligned}
S''\{\delta\} \approx \frac{\rho}{T}\Bigg[& \nu\int_0^\delta (\partial U/\partial y)^2 dy - \int_0^\delta (\overline{uv})(\partial U/\partial y)dy \\
& - \int_0^\delta \left[\overline{(u^2)} - \overline{(v^2)}\right](\partial U/\partial x)dy \\
& - (d/dx)\int_0^\delta U(1/2)\overline{(q^2)}dy \\
& - (1/2)\overline{v_\delta\left[(u_\delta^2) + (v_\delta^2) + (w_\delta^2)\right]} - \overline{v_\delta p_\delta}\Bigg]
\end{aligned}
\tag{6.2}
$$

After Eq. 6.1 was applied to the first four terms of Eq. 6.2, they were converted into their respective dissipation coefficients, C_d, by means of Eq. 2.7, and plotted in Fig. 6.1. Each term is shown as they apply to the total by including their respective sign (+/-) as shown in the equation. Also, as mentioned above, the last two terms from Eq. 6.2 have been removed from the equation as they are neglible in magnitude in relation to the total, as seen in Walsh *et al.* [63].

Upon plotting the dissipation coefficient, C_d, it appears from Fig. 6.1a that the boundary layer of the ZPG without TG case is in fact remaining laminar throughout, and not going through a transition process. This can be understood with the only term with magnitude is the viscous term (i.e., the first term in Eq. 6.2). When Figure 6.1b and 6.1c are held against the DNS results found in Fig. 6 of Walsh [63] (duplicated here in Fig. 6.2 for simplicity), and considering Figure 6.6 (discussed and shown below), both cases are beginning their respective transition processes near, or just downstream from, the leading edge of the plate. This is seen by the increase in the Reynolds shear stress term (dotted line), as the turbulent eddies begin to increase through the transition process and into the turbulent boundary layer. In fact, the Reynolds shear stress term begins the increase *before* the traditional onset of transition location of minimum C_f as seen in Fig. 4.5; where the local minimum of C_f corresponds to the $\sqrt{Re_x}$ values seen on the abscissa of Fig. 6.1 as 650, 170, and 150 for the ZPG without TG, ZPG with TG, and APG with TG flow configurations,

respectively. Conversely, the viscous term is decreasing (or has decreased in the APG w/ TG case) enough to show the trade off in the viscous contributions to the turbulent contributions – again as seen in Fig. 6.2. An interesting feature of the ZPG with TG flow configuration in Fig. 6.1 is the intersection of the Mean and Reynolds Shear Stress terms coincide almost exactly with the local minimum of the C_f curve. A similar feature can be seen in the APG with TG flow configuration, but slightly downstream of the local minimum prediction of the C_f curve. This leads to the conclusion that within bypass transition of a boundary layer, the use of entropy generation can help predict the transition location. Further, in all three flow conditions, the later two terms (i.e., Normal Stress production and Energy flux) in Eq. 2.5 are seen to be small in magnitude compared to the former two terms discussed previously. This is again consistent with the DNS results from [63].

An uncertainty analysis was performed on the results found in Fig. 6.1c by using the surface method as described by Timmins *et al.* [54]. The uncertainty on streamwise velocity measurements was calculated and a typical profile was seen as shown in Fig. 6.3 – where the uncertainty increases within the boundary layer. The uncertainty in velocity measurements was then carried through Eqs. 2.5 and 2.7, step-by-step, by means of the RMS method in Kline and McClintock [26]. The uncertainty in the integration in Eq. 2.5 was carried out by the trapezoidal rule, and the RMS method was applied in both the calculation of the individual rectangles, and in the summation process to compute the integral itself. A typical uncertainty of +/- 9.5% the total dissipation coefficient by means of the areal entropy generation rate was observed (black line in Fig. 6.1).

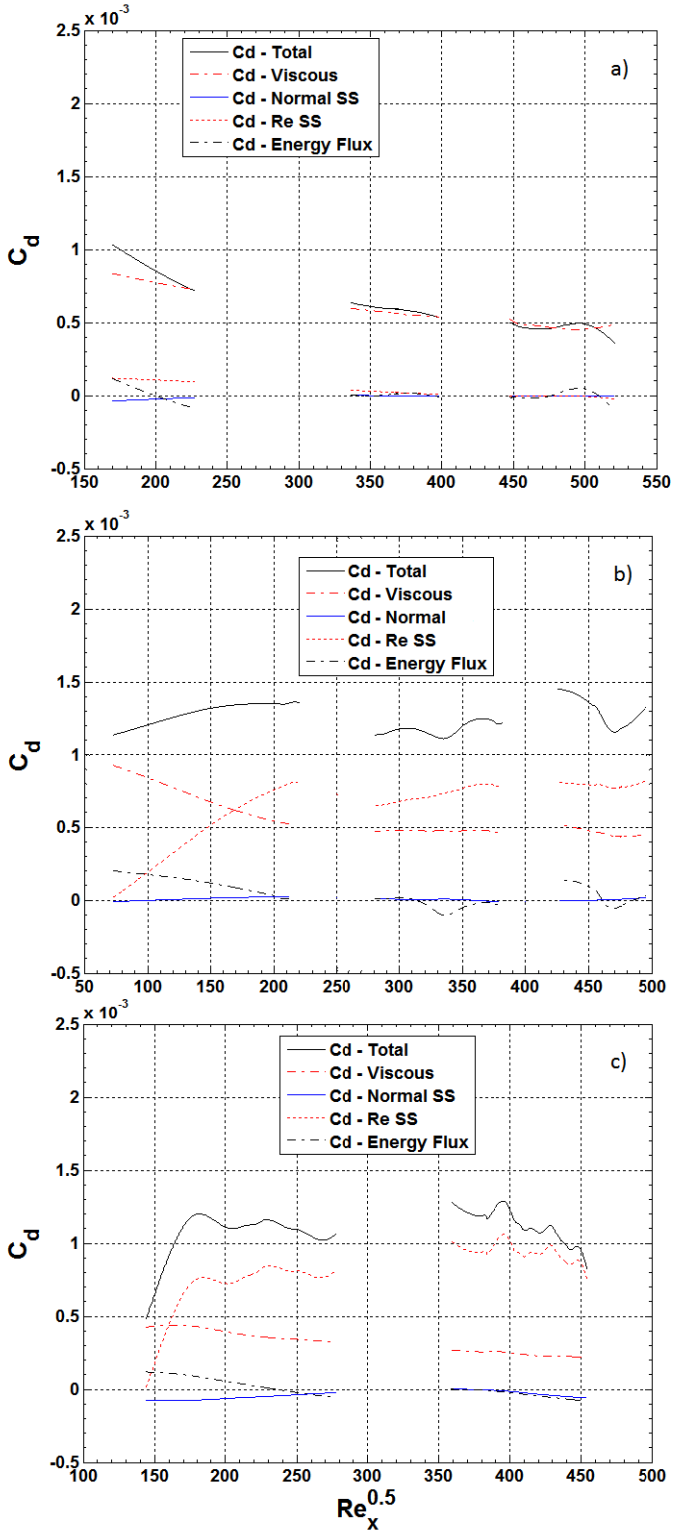

Figure 6.1: Dissipation coefficient, C_d, for each flow condition. Also, individual contributions of each term of Eq. 2.5. A slight smoothing was applied. a) ZPG w/out TG, b) ZPG w/ TG, and c) APG w/ TG.

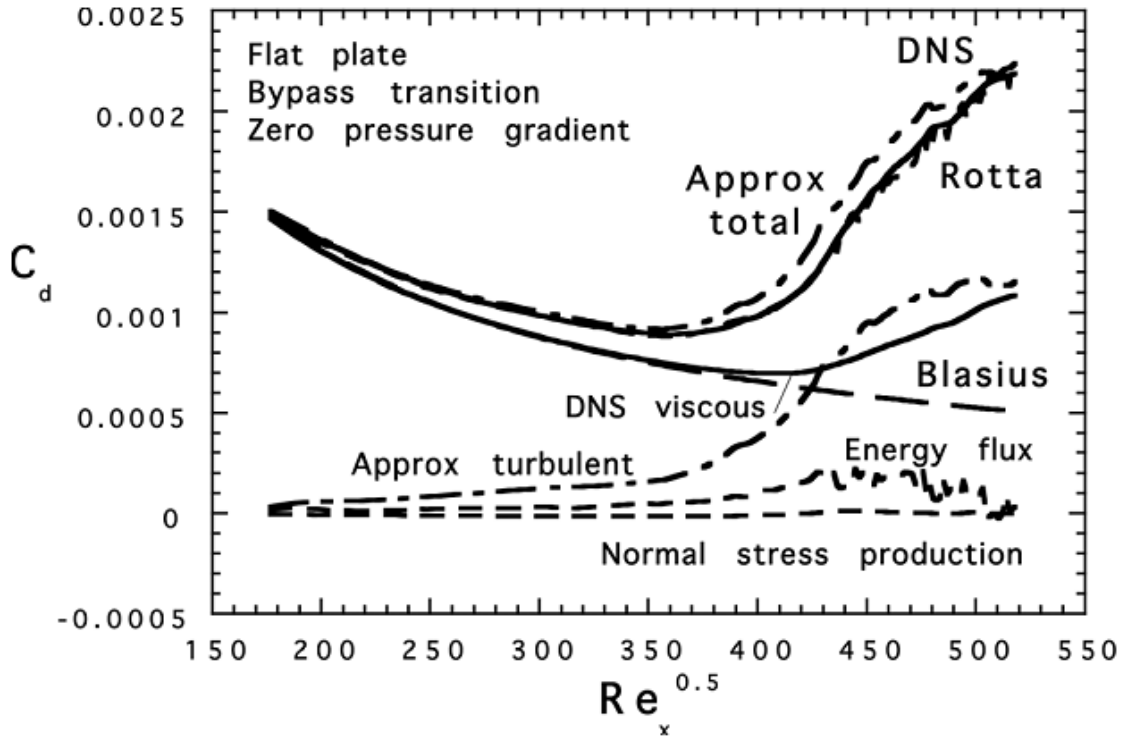

Figure 6.2: The streamwise profiles of the dissipation coefficient, C_d. $FSTI_x = 4.7\%$. As predicted by DNS in Walsh *et al.* [63]. For comparison to Fig. 6.1.

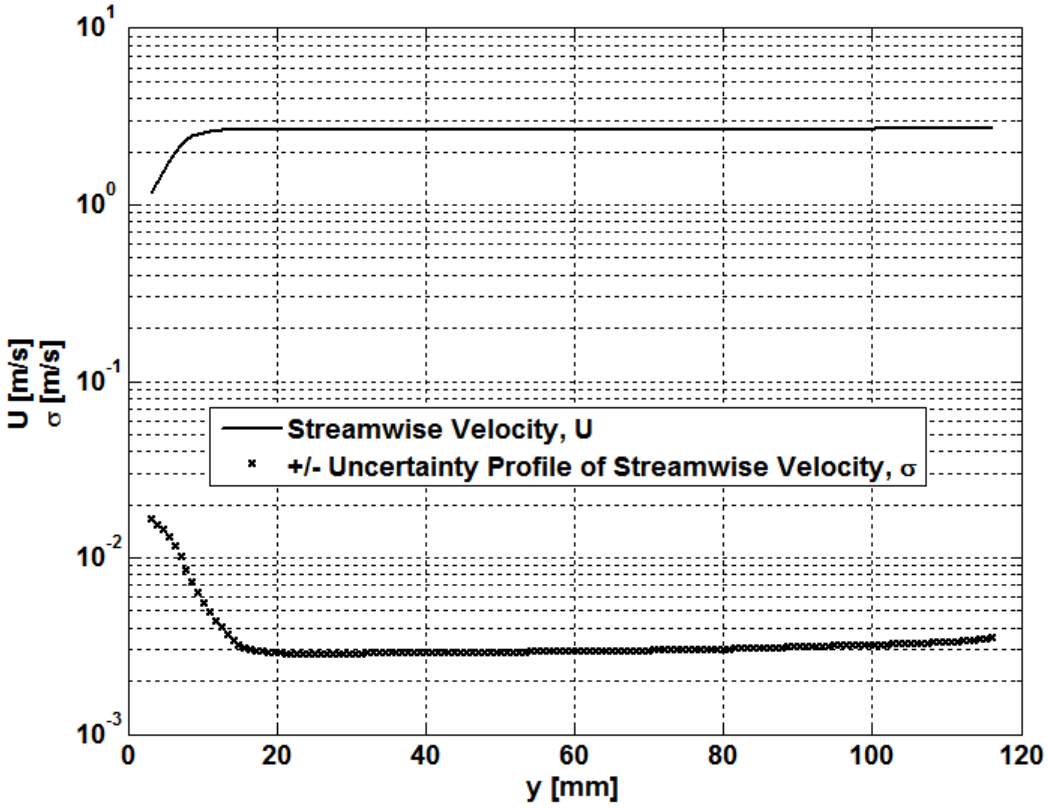

Figure 6.3: Typical uncertainty profile of streamwise velocity for the APG flow configuration at x = 0.15 m.

6.2 Behavior of Pointwise Entropy Generation Rate within Pre-Transitional and Bypass Transitional Wall Bounded Flow

To better understand the behavior of the turbulent contributions to pointwise entropy generation rate, S''' (and therefore S'', S', and S), as defined in Eq. 2.3, the author utilized the DNS calculations from McEligot *et al.* [36], Walsh *et al.* [63], and the experimental hot-wire measurements from Klebanoff [24]. In terms of the pointwise entropy generation rate there are two contributions, direct and indirect. These are represented in Eq. 2.3 as $\mu\Phi$ and $\rho\epsilon$, respectively. These terms come in the form of

the spatial gradients of the time averaged velocities (e.g. $\mu\Phi = (dU/dy)^2 + ...$), where capital U, V, etc. mean time averaged velocities. This is then followed by the squared, mean, spatial gradients of the instantaneous velocities (e.g. $\rho\epsilon = \overline{(du/dx)^2}+...$), where lowercase u, v, etc. signify the instantaneous measurement of the velocity.

6.2.1 DNS calculations of a laminar to transitional boundary layer

Walsh *et al.* have shown at locations of onset to transitional flow, and at low y^+ values, the turbulent contributions (indirect) were approximately 1/10th the total rate of entropy being generated, and around a y^+ of 50 to 60 the rates between viscous and turbulent contributions became equal, and pratically negligible. This means that a majority of the entropy being generated at pre-transitional to transitional locations are at a very close proximity to the wall, and both taper off rather quickly. These ideas can be seen readily in Fig. 6.4, where the breakdown of the different contributions – and the corresponding approximates (see Eq. 2.4) – are plotted as a wall normal profile in wall coordinates.

6.2.2 Air tunnel measurements from a 'X' probe hot-wire anemometer of a fully turbulent boundary layer

In contrast, the Klebanoff experimental results [24] are for a well developed turbulent boundary layer ($Re_x = 4.2 \cdot 10^6$) over a flat plate in air. Even more so, the first two feet of the plate were covered in rough sandpaper to further 'trip' the boundary layer into the turbulent state. The hot wire measurements are presented in Fig. 14 of the paper – in the form of instantaneous squared and averaged spatial gradients. Further, a streamwise velocity profile from the wall to the boundary layer are presented in Fig. 3 of the same paper. These figures were digitized and applied directly to Eqs. 2.2 and 2.1, respectively.

There was only a single 'X' hot-wire probe, therefore the time derivatives were

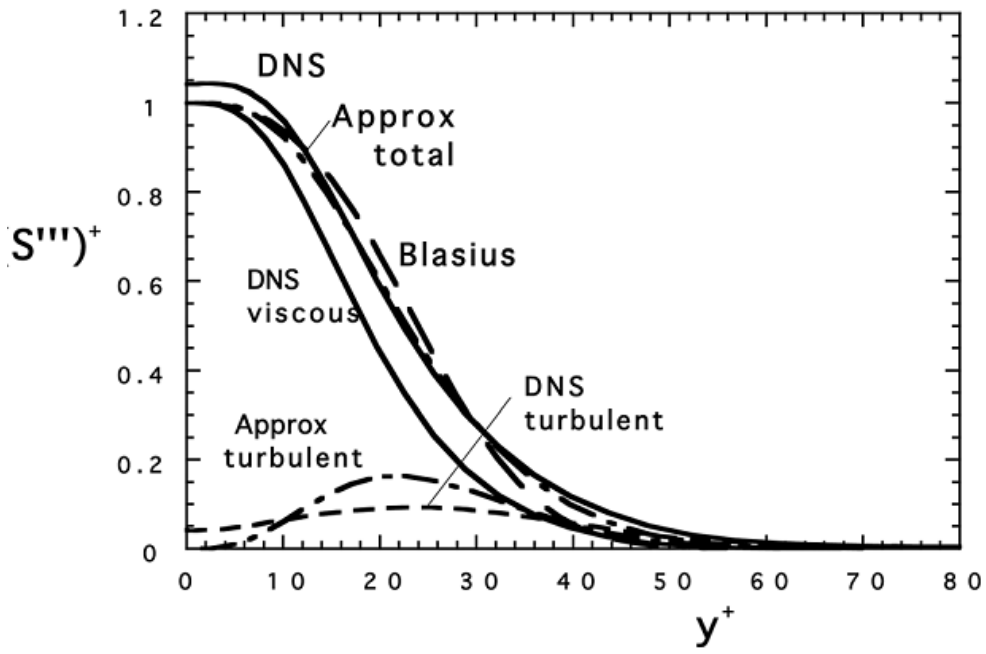

Figure 6.4: The profiles of pointwise entropy generation rates (viscous, turbulent, and approximate) in a pre-transitional boundary layer. $\sqrt{Re_x} = 350$ and $FSTI_x = 4.7\%$. As predicted by DNS in Walsh *et al.* [63]

converted to the spatial derivatives by assuming the accuracy of the space-time transformation. For example,

$$\overline{\left(\frac{\partial u}{\partial x}\right)^2} = \frac{1}{U^2}\overline{\left(\frac{\partial u}{\partial t}\right)^2} \tag{6.3}$$

where U is local mean velocity. Further, in order to utilized these measurements in Eq. 2.3 were rewritten by Rotta [46] into

$$\begin{aligned}\rho\epsilon = \mu\Bigg[&\overline{\left(\frac{\partial u}{\partial x}\right)^2} + \overline{\left(\frac{\partial v}{\partial x}\right)^2} + \overline{\left(\frac{\partial w}{\partial x}\right)^2} + \overline{\left(\frac{\partial u}{\partial y}\right)^2} + \overline{\left(\frac{\partial v}{\partial y}\right)^2} + \overline{\left(\frac{\partial w}{\partial y}\right)^2} \\ &+ \overline{\left(\frac{\partial u}{\partial z}\right)^2} + \overline{\left(\frac{\partial v}{\partial z}\right)^2} + \overline{\left(\frac{\partial w}{\partial z}\right)^2} + \frac{d^2}{dy^2}\overline{v^2}\Bigg].\end{aligned} \tag{6.4}$$

With that being said, there was a need for a few assumptions in order to calculate total pointwise entropy generation rate from Klebanoff's paper. First, the streamwise velocity profile was only given at one location over the plate, therefore the direct

dissipation, Eq. 2.1, was approximated with

$$\mu\Phi \approx \mu \left(\frac{dU}{dy}\right)^2 \tag{6.5}$$

where the latter terms have been dropped in Eq. 2.1 due to their relatively low magnitude. In other words, the streamwise normal velocity gradient is the most significant.

Further, as all ten terms of Eq. 6.4 were not present in Klebenoff's paper, great care was taken as to a few of the assumptions needed to compute the remaining squared, averaged, instantaneous spatial gradients. Rotta [46] discusses a few of the physical behaviors of the said spatial gradients utilized in Eq. 6.4. That is, at the wall (y = 0), all squared and averaged spatial gradients in the x- and z-direction are equal to zero from the nature of the no-slip condition. In the wall normal direction, du/dy and dw/dy at the wall are equal to a non-zero finite value. In contrast, dv/dy is in fact zero at the wall from continuity

$$\left.\frac{dv}{dy}\right|_w = -\left.\frac{du}{dx}\right|_w - \left.\frac{dw}{dz}\right|_w = 0$$

where, as mentioned above, the no slip condition brings gradients in the x- and z-directions to zero at the wall.

These assumptions were applied using

$$\overline{\left(\frac{\partial u}{\partial x}\right)^2}, \overline{\left(\frac{\partial v}{\partial x}\right)^2}, \overline{\left(\frac{\partial w}{\partial x}\right)^2}, \overline{\left(\frac{\partial u}{\partial y}\right)^2}, \text{ and } \overline{\left(\frac{\partial u}{\partial z}\right)^2}$$

as the known quantities, and applying them to the remaining four unknowns by

$$\overline{\left(\frac{\partial v}{\partial y}\right)^2} = \frac{1}{2}\overline{\left(\frac{\partial u}{\partial z}\right)^2},$$

$$\overline{\left(\frac{\partial w}{\partial y}\right)^2} = \overline{\left(\frac{\partial u}{\partial y}\right)^2},$$

$$\overline{\left(\frac{\partial v}{\partial z}\right)^2} = \overline{\left(\frac{\partial u}{\partial z}\right)^2}, \text{ and}$$

$$\overline{\left(\frac{\partial w}{\partial z}\right)^2} = \frac{1}{2}\overline{\left(\frac{\partial u}{\partial z}\right)^2}.$$

Lastly, the term $d^2(\overline{v^2})/dy^2$ was calculated by central differencing Fig. 4 of the Klebanoff paper [24].

The pointwise entropy generation rate of both turbulent and viscous contributions from Klebanoff can be seen as a wall normal profile in Fig. 6.5. Also plotted in Fig. 6.5, as a reference, are the DNS results from McEligot *et al.* [36]. As for the comparison between locations in the turbulent boundary layers, the Klebanoff experimental results are at a location with $Re_\theta = 7445$; while the DNS results from McEligot are at $Re_\theta = 1410$. Furthermore, both flows have a negligible freestream turbulence and zero (or negligible) pressure gradient.

Regarding the structure of the curves in Fig. 6.5, the viscous contribution reduced down to almost nothing rather quickly at a y^+ of approximately 60–70. Both viscous contributions, from both datasets, are practically the same. This is identical to the observation made by McEligot *et al.* [36], insomuch that the viscous contributions in a turbulent boundary layer are independent of Reynolds number. Also, the turbulent contributions at close proximity to the wall were less than 1/10th the viscous contributions of entropy generation rate.

This appears to be consistent with the laminar boundary layer shown previously by Walsh in Fig. 6.4. The governing contrast of pointwise entropy generation rate between these two completely separate boundary layers is the magnitude of the turbulent contribution term, $\rho\epsilon$. Looking specifically at the Klebanoff experimental data – since this was a well developed turbulent boundary layer – the pointwise entropy generation rate doesn't "zero" out until around $y^+ = 1000$ – with the laminar station

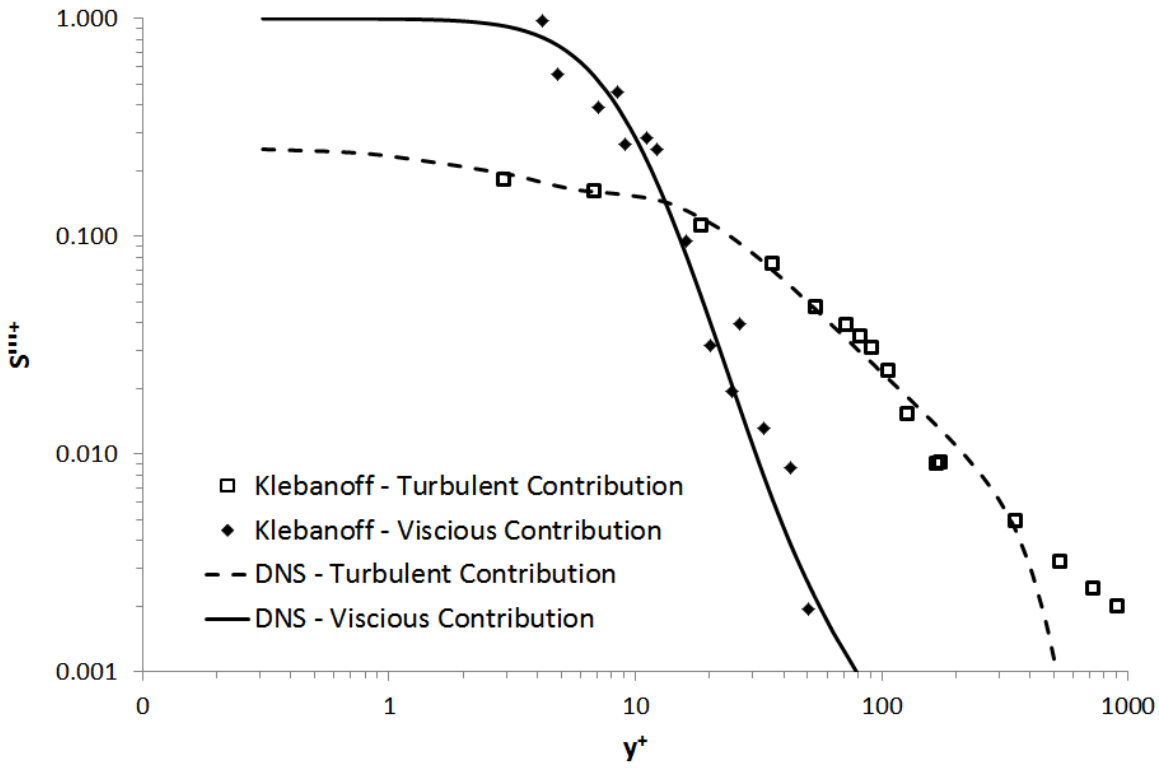

Figure 6.5: Wall normal profile of the pointwise entropy generation rate as calculated by the author from Klebanoff [24] (symbols) at a $Re_\theta = 7445$. Also, DNS results of the same calculated by McEligot *et al.* [36] (lines) at a $Re_\theta = 1410$.

shown previously 'zeroed' out around $y^+ = 70 - 80$.

To further emphasize this principle, the Klebanoff data was integrated to achieve the total areal entropy generation rate, S''. This showed the turbulent contribution was approximately 1/2 the total entropy generation rate within the boundary layer. In other words, the integration of pointwise entropy generation rate, S''', from the wall to the boundary layer thickness was approximately 1/2 turbulent contributions, and approximately 1/2 viscous contributions. This is seen as the area under the curve in Fig. 6.5 (which is slightly misleading with the log-log scale.) This means that even though a majority of the entropy being generated is within a very close proximity to the wall due to viscous contributions (for both a laminar and turbulent boundary layer) [46], the turbulent eddies in a well developed boundary layer are contributing a significant amount *throughout* the boundary layer.

In summary, the contrast between the Walsh *et al.* DNS calculations (Fig. 6.4) to that of the Klebanoff experimental work (Fig. 6.5) was wherein the profiles were located in relation to the flow conditions. At the location presented in Fig. 6.4, Walsh *et al.* was in a laminar boundary layer (that is, just at the location of immediate transition), and both viscous and turbulent contributions reduce to near zero by a $y^+ = 70$. Conversely, the Klebanoff data are within a turbulent boundary layer, and the turbulent contribution to S''' is never totally 'zero' until outside the boundary layer (presumably).

This same demonstration can also be seen in the MIR dataset in Fig. 6.1b and c by comparing the viscous curve (dash-dot) to the Reynolds shear stress curve (dashed). The Reynolds shear stress curve ramps up to a finite value through the transition region and beyond. Thus showing the trade off in entropy generation rate from direct diffusion in the laminar boundary layer to indirect diffusion in a fully developed turbulent boundary layer. The demonstration now looks specifically at the transitional region of the boundary layer.

6.3 Pointwise Entropy Generation Rate from the MIR Dataset

Now that the behavior of the viscous and turbulent contributions has been shown by others, pointwise entropy generation rate was computed for the MIR dataset. Unfortunately, it was seen that the calculations for the turbulent contribution of pointwise entropy generation rate had too much uncertainty and/or noise, and was therefore on the order of magnitude 100 too high. However, it was still important to see the behavior of the pointwise entropy generation rate through the transition process experimentally, so it was decided to move forward with just the viscous contribution from Eq. 2.3, that is $\mu\Phi$. Figure 6.6 is the development of time-averaged distributions of the viscous contribution of $(S''')^+$ versus y^+ down the length of the plate (increasing values of $\sqrt{Re_x}$). Where $(S''')^+$ is defined only by equation 2.1 mul-

tiplied by $\nu T/\rho u_\tau^4$. The velocity vector pitch on the PTV grid from the MFOV scale was 0.05 mm - which is approximately unity with the local Kolmogorov length scale. In the locations of an erroneous vector - or no vector at all - the vector was treated as a "NaN". This affected the time-mean quantities utilized in $\mu\Phi$ as well, but of the 4,000 image pairs taken it was found that typically 2000 vectors were present to compute the averages at each location of the post-processed time-averaged vector map.

Had the derivatives been incorporated into the plots found in Fig. 6.6, they would have presumably been at the 10% range of the total entropy generation rate within the viscous sublayer, as was seen in Walsh *et al.* [63] and Klebanoff [24]. Interestingly enough, the squared mean gradients of the flow where showing the right trends (according to theory [46]), they were just not at the right magnitude, presumably from the uncertainty in the PTV measurements. A look at the squared mean gradient profiles can be seen in the appendix.

When Fig. 6.6 was compared to Fig. 5 of Walsh *et al.* [63] (placed here in Fig. 6.7 for simplicity) the trends were very similar, even though the turbulent contribution term, $\rho\epsilon$, was removed from the current work. This is consistant with the trade off seen previously between direct and indirect dissipation as the boundary layer goes through the transisiton process. The pre-transitional profile (solid line in the figures) is larger and reduces at a lower slope (which is more pronounced in the APG w/ TG flow, 6.6b). At the onset of transition the profile comes in towards the lower y^+ values, and continues to reduce in the same manner, at downstream locations. This is from the exchange between viscous and turbulent dissipation. Further, since these curves are non-dimentionalized with essentially the shear stress at the wall, by definition, they can all be extrapolated to 1 at $y^+ = 0$. This gives a complete understanding of the viscous contributions in pointwise entropy generation rate from the wall to the freestream flow through the transition process. The ZPG without TG case is

not shown in Fig. 6.6, as the flow conditions did not exhibit a transition process. Furthermore, laminar boundary layers with negligible freestream turbulence can be calculated to solve for S'''' using the Blasius or Pohlhousen solutions [27].

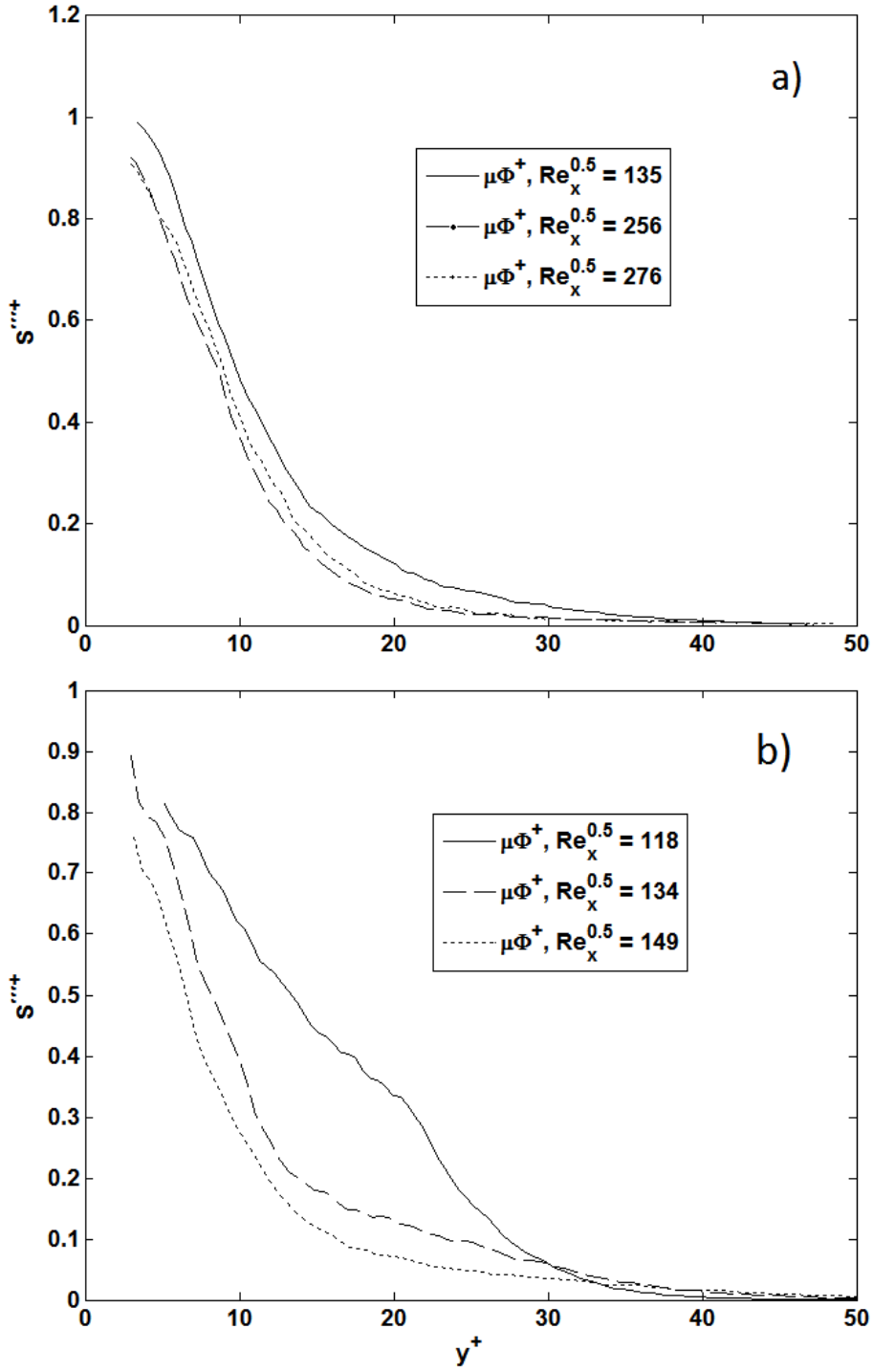

Figure 6.6: $(S''')^+$ profiles at streamwise stations $\sqrt{Re_x}$ in the transitional region for both cases with a turbulence generator. a) ZPG with TG. b) APG with TG. ZPG without TG not shown.

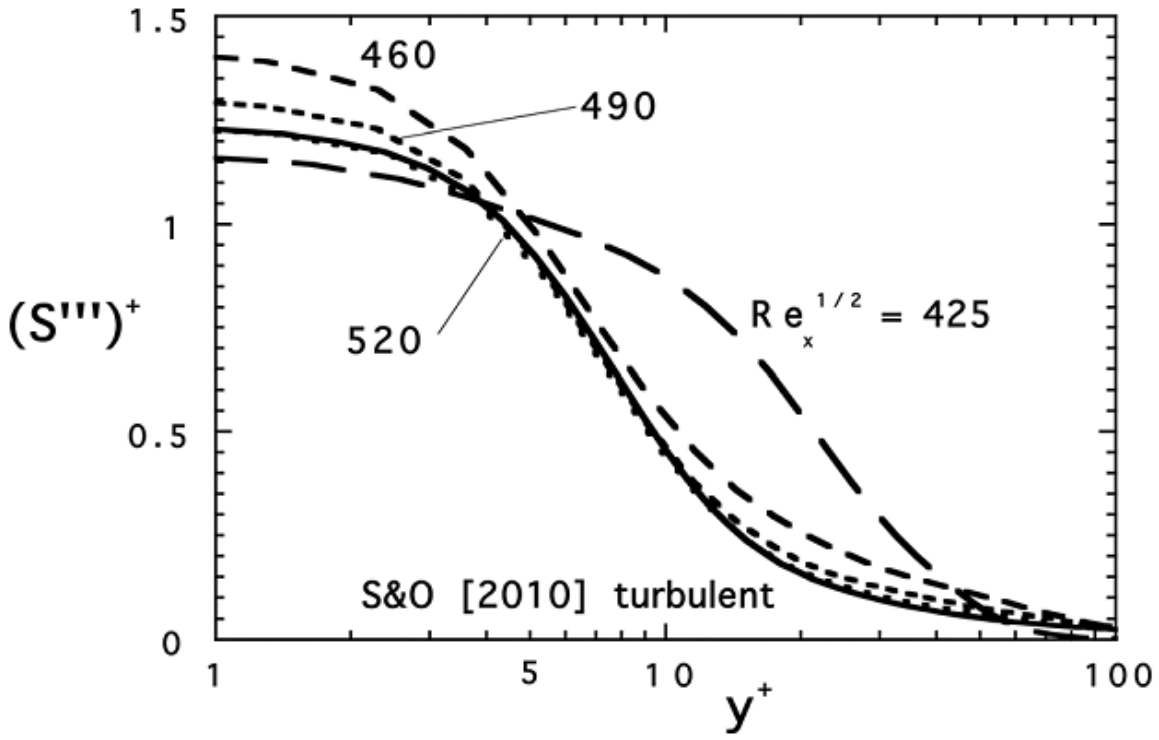

Figure 6.7: Time- and Spanwise-averaged total $(S''')^+$ profiles at streamwise stations ($\sqrt{Re_x}$) within the transitional region, compared to Schlatter and Örlü [48] from a fully turbulent boundary layer. Figure from Walsh *et al.*
[63].

Chapter 7

Conclusions

To further understand the entropy generation rates in a bypass boundary layer transition process, a study was performed at the Matched Index of Refraction Flow Facility located at the Idaho National Laboratory (INL). A flat plate was installed within the test section of the MIR, and three flow configurations were utilized to either help comprehend or measure the entropy generation rate within a "bypass" transitional boundary layer. These flow configurations were zero pressure gradient with out turbulence generator (ZPG without TG), zero pressure gradient with turbulence generator, and adverse pressure gradient with turbulence generator (APG with TG).

Previous work on entropy calculations have been performed, but none have looked specifically at bypass, transitional, boundary layer flow with the relatively high free stream turbulence intensities (e.g. $\sim 8\%$) achievable in the MIR. Neither has the study of entropy generation rate behavior within the transitional region of the boundary layer within an adverse pressure gradient been seen before experimentally. Further, the optical techniques utilized in the current work was able to achieve data within a $y^+ < 2.5$ – a considerable improvement from $y^+ = 10$, or greater, by others.

The comparisons between the bypass transitional measurements presented in this work to that of published DNS results show a very similar trend. The trends show the turbulent contributions of pointwise entropy generation rate trading off with the viscous contributions through the transition process and beyond. A large majority of the contributions come within a $y^+ < 30$, but within the transitional region of the boundary layer a trade off between viscous and turbulent dissipation takes place where an increasing amount of the total entropy generation rate is seen throughout the boundary layer. This is most prevalent within the case of the APG with TG

flow configuration as the viscous contribution continues to decrease throughout the transitional and turbulent boundary layer, but the turbulent contribution continues to rise. Where, in contrast, the ZPG flow configuration still has an increase in the turbulent contribution as the boundary layer grows, but the viscous contribution to pointwise entropy generation stays constant.

Work was also done to help improve particle image velocimetry (PIV) measurements in high shear regions very near a wall interface. The particles utilized to seed the flow in this region are found to be biased *away* from the interface, and lead to biased measurements of the velocity (i.e., higher than to be expected). This provided the need to correct for the biased error in the measurement, systematically, by using the average centroid location of the image intensity as the "true" location of the reported velocity measurement. This centroid corrected method was applied to two flow configurations, and improvements to the velocity gradient at or near the wall were seen. For the ZPG without TG dataset the velocity gradient at the wall was improved from 53.5% to 8.7% when compared to the Blasius profile. In the same flow, the velocity measurement location (closest to the wall) was improved from 27.9% error down to 1.8% error when compared to the same Blasius profile. For the vertical heated plate dataset there was a 41.9% improvement to the velocity gradient at the wall; while the measurement location of the velocity (closest to the wall) was seen to improve by 16.2%.

References

[1] Abu Ghannam, B. J., and Shaw, R. Natural transition of boundary layers – the effects of turbulence, pressure gradient, and flow history. *Journal of Mechanical Engineering Science 22*, 5, 213–228.

[2] Ames, F. E., and Plesniak, M. W. The influence of large-scale, high-intensity turbulence on vane aerodynamic losses, wake growth and the exit turbulence parameters. *J. Turbomachinery 119* (1997), 182–192.

[3] Bejan, A. *Entropy generation through heat and fluid flow.* New York: Wiley.

[4] Blasius, H. Grenzschichten in flüssigkeiten mit kleiner reibung. *Z. Math. Phys. 56* (1908), 1–37.

[5] Bradshaw, P. The turbulence structure of equilibrium boundary layers. *J. Fluid Mech. 29* (1967), 625–645.

[6] Brandt, L., Schlatter, P., and Henningson, D. S. Transition in boundary layers subject to free-stream turbulence. *J. Fluid Mech. 517* (2004), 167–198.

[7] Budwig, R. S. Refractive index matching methods for liquid flow investigations. *Exp. Fluids 17* (1994), 350–355.

[8] Budwig, R. S., and Westin, R. Measurement of oil properties. *INL Internal Report* (2011), 1–14.

[9] Comte-Bellot, G., and Corrsin, S. Simple Eulerian time correlation of full-and narrow-band velocity signals in grid-generated, turbulence. *Journal of Fluid Mechanics 48*, 02 (July 1971), 273–337.

[10] Dunham, J. Predictions of boundary layer transition on turbomacinary blades. *Boundary layer effects in turbomachines 164* (1972), 55–71.

[11] Fransson, J. H. M. Leading edge design process using a commercial flow solver. *Experiments in Fluids 37*, 6 (Oct. 2004), 929–932.

[12] Gad-el-Hak, M., and Corrsin, S. Measurements of nearly isotropic turbulence behind a uniform jet grid. *J. Fluid Mech. 62* (1974), 115–143.

[13] George, J., Owen, L. D., Xing, T., McEligot, D. M., Crepeau, J. C., Budwig, R. S., and Nolan, K. P. Entropy generation in bypass transitional boundary layer flows. *Journal of Hydrodynamics, Ser. B 26*, 5, 669–680.

[14] Ghasemi, E., McEligot, D. M., Nolan, K. P., Crepeau, J., and Budwig, R. S. Entropy generation in a transitional boundary layer region under the influence of freestream turbulence using transitional rans models and dns. *International Communications in Heat and Mass Transfer 41* (2013), 10–16.

[15] Gilmore, R. *The shadow of entropy, Scrooge's Cryptic Carol*. Copernicus (Springer-Verlag).

[16] Griffin, P. C., Davies, M. R. D., O'Donnell, F. K., and Walsh, E. The Effect of Reynolds Number, Compressibility and Free Stream Turbulence on Profile Entropy Generation Rate. *ASME Turbo Expo 2002: Power for Land, Sea, and Air* (Jan. 2002), 61–69.

[17] Hanson, R. E., Buckley, H. P., and Lavoie, P. Aerodynamic optimization of the flat-plate leading edge for experimental studies of laminar and transitional boundary layers. *Experiments in Fluids 53*, 4 (June 2012), 863–871.

[18] Harris, J. *A Computational Fluid Dynamics Validation Experiment for Forced and Mixed Convection on a Vertical Heated Plate*. Ph.d. thesis, Utah State University, Logan, UT, 2014.

[19] Harris, J. R., Lance, B. W., and Smith, B. L. Experimental validation data for CFD of forced convection on a vertical flat plate. *J. Fluid Eng.* (accepted for publication 2015).

[20] Hill, J. L. Sustainable? Says who? *Mech. Engr.* (September 2008), 10.

[21] Jacobs, R. G., and Durbin, P. A. Simulations of bypass transition. *J. Fluid Mech. 428* (2001), 185–212.

[22] Johansson, T. G., Medhi, F., and Naughton, J. W. Some problems with near-wall measurements and the determination of wall shear stress. *25th AIAA Aerodynamic Measurement Technology and Ground Testing Conference* (2006), 5–8.

[23] Kähler, C. J., Scholz, U., and Ortmanns, J. Wall-shear-stress and near-wall turbulence measurements up to a single pixel resolution by means of long-distance micro-piv. *Exp. in Fluids 41* (2006), 327–341.

[24] Klebanoff, P. S. Characteristics of turbulence in a boundary layer with zero pressure gradient. *NACA report 1247* (1955), 1135–1153.

[25] Klebanoff, P. S. Effect of freestream turbulence on the laminar boundary layer. *Bull. Amer. Physical Soc. 10* (1971), 1323.

[26] Kline, S. J., and McClintock, F. A. Descibing uncertainties in single-sample experiments. *Mechanical Engineering 75* (1953), 3–8.

[27] Kline, S. J., Reynolds, W. C., Schraub, F. A., and Runstadler, P. W. The structure of turbulent boundary layers. 741–773.

[28] Kock, F., and Herwig, H. Entropy production calculation for turbulent shear flows and their implementation into cfd codes. *Int. J. Heat Fluid Flow 26* (2005), 672–680.

[29] Liu, Y., Zaki, T. A., and Durbin, P. A. Boundary-layer transition by interaction of discrete and continuous modes. *J. Fluid Mech. 604* (2008), 199–233.

[30] Liu, Y., Zaki, T. A., and Durbin, P. A. Floquet analysis of secondary instability of boundary layers distorted by klebanoff streaks and tollmien-schlichting waves. *Phys. Fluids 20* (2008), 1–16.

[31] Matsubara, M., and Alfredsson, P. H. Disturbance growth in boundary layers subjected to free-stream turbulence. *J. Fluid Mech. 430* (2001), 149–168.

[32] Mayle, R. E. The role of laminar-turbulent transition in gas turbine engines. *J. Turbomachinery 113* (1991), 509–537.

[33] McEligot, D. Personal correspondence, 2012.

[34] McEligot, D. M., Brodkey, R. S., and Eckelmann, H. Laterally converging duct flows: Part 4. temporal behavior in the viscous layer. *J. Fluid Mech. 634* (2009), 433–461.

[35] McEligot, D. M., and Eckelmann, H. Laterally converging duct flows: Part 3. mean turbulence structure in the viscous layer. *J. Fluid Mech. 549* (2006), 25–59.

[36] McEligot, D. M., Walsh, E. J., Laurien, E., and Spalart, P. R. Entropy generation in the viscous parts of a turbulent boundary layer. *J. Fluids Engr. 130* (2008), 1–12.

[37] McIlroy, H. M., and Budwig, R. S. The boundary layer over turbine blade models with realistic rough surfaces. *J. Turbomachinery 129* (2007), 318–330.

[38] Narasimha, R. The laminar-turbulent transition zone in the boundary layer. *Prog. Aerosp. Sci. 22* (1985), 29–80.

[39] Nolan, K. P., and Walsh, E. J. Particle image velocimetry measurements of a transitional boundary layer under free stream turbulence. *J. Fluid Mech. 702* (2012), 215–238.

[40] Nolan, K. P., Walsh, E. J., McEligot, D. M., and Volino, R. J. Predicting entropy generation rates in transitional boundary layers based on intermittency. *J. Turbomachinery 129* (2007), 512–517.

[41] Nolan, K. P., and Zaki, T. A. Conditional sampling of transitional boundary layers in pressure gradients. *J. Fluid Mech. 728* (2013), 306–339.

[42] Owen, L. D., George, J., Xing, T., McEligot, D. M., Crepeau, J. C., and Budwig, R. S. Laminar boundary layer entropy generation over a flat plate under favorable and adverse pressure gradients. *Entropy (To be submitted)* (2015).

[43] Reynolds, W. C. *Thermodynamics*, 2nd ed. McGraw-Hill.

[44] Roach, P. E. The generation of nearly isotropic turbulence by means of grids. *International Journal of Heat and Fluid Flow 8* (1987), 82–92.

[45] Rose, M. G. What should we measure? an aero-engine turbine aero-dynamic perspective. *XIV Bi-annual Symp. Meas. Techniques in Transonic and Supersonic Flow in Cascades and Turbomachines, Limerick* (September 1998).

[46] Rotta, J. C. Turbulent boundary layers in incompressible flow. *Progress in Aeronautical Sciences 2* (1962), 1–219.

[47] Schlatter, P., Brandt, L., de Lange, H. C., and Henningson, D. S. On streak breakdown in bypass transition. *Phys. Fluids 20* (2008), 1–15.

[48] Schlatter, P., and Örlü, R. Assessment of direct numerical simulation data of turbulent boundary layers. *Journal of fluid mechanics 659* (2010), 116–126.

[49] Schlichting, H. *Boundary layer theory*, 8 ed. New York: McGraw-Hill, 2000.

[50] Spalding, D. B. A single formula for the 'Law of the Wall'. *J. of Applied Mech. 28*, 3 (1961), 455–458.

[51] Stoots, C. M., Becker, S., Condie, K. G., Durst, F., and McEligot, D. M. A large-scale matched-index-of-refraction flow facility for lda studies of complex geometries. *Exp. Fluids 30* (2001), 391–398.

[52] Suder, K. L., O'Brien, J. E., and Reshotko, E. *Experimental study of bypass transition in a boundary layer.* National Aeronautics and Space Administration, [Washington, DC]; [Springfield, Va.], 1988.

[53] Theunissen, R., Scarano, F., and Riethmuller, M. L. On improvement of piv image interrogation near stationary interfaces. *Exp. Fluids 45* (2008), 557–572.

[54] Timmins, B. J., Wilson, B. W., Smith, B. L., and Vlachos, P. P. A method for automatic estimation of instantaneous local uncertainty in particle image velocimetry measurements. *Exp. Fluids 53* (2012), 1133–1147.

[55] Unsera G., Vernet, A. F. J. Condiserations and improvements of the analysing algorithms used for time resolved piv of wall bounded flows. *Proceedings of the 12th international symposium on applications of laser techniques to fluid mechnaics.* (2004), 11–15.

[56] Uzol, O., and Camci, C. The effect of sample size, turbulence intensity and the velocity field on the experimental accuracy of ensemble averaged piv measurements. In *4th International Symposium on Particle Image Velocimetry, Goettingen, Germany, September* (2001), pp. 17–19.

[57] Volino, R. J., P., S. M., and Pratt, C. M. Conditional sampling in a transitional boundary layer under high freestream turbulence conditions. *J. Fluids Eng. 125* (2003), 28–37.

[58] Vukoslavcevic, P., and Wallace, J. M. The simultaneous measurement of velocity and temperature in heated turbulent air flow using thermal anemometry. *Meas. Sci. Technol 13* (2002), 1615–1624.

[59] Walsh, E., Myose, R., and Davies, M. A Prediction Method for the Local Entropy Generation Rate in a Transitional Boundary Layer With a Free Stream Pressure Gradient. *ASME Turbo Expo 2002: Power for Land, Sea, and Air 3* (Jan. 2002), 637–646.

[60] Walsh, E. J., and Davies, M. R. D. Compressibility effects on the entropy generation rate in steady adiabatic transitional boundary layers. *Proc., Fifth European Conf. Turbomachinery, Fluid Dynamics and Thermodynamics, Prague, Czech Republic* (2003), TT01–201.

[61] Walsh, E. J., and McEligot, D. M. Relation of entropy generation to wall 'laws' for turbulent flows. *Int. J. Comp. Fluid Dynamics 22* (2008), 649–657.

[62] Walsh, E. J., and McEligot, D. M. A new correlation for entropy generation in turbulent shear layers. *Int. J. Fluid Mech. Research 36* (2009), 566–572.

[63] Walsh, E. J., McEligot, D. M., Brandt, L., and Schlatter, P. Entropy Generation in a Boundary Layer Transitioning Under the Influence of Freestream Turbulence. *Journal of Fluids Engineering 133*, 6 (June 2011), 1–10.

[64] Walsh, E. J., Nolan, K. P., McEligot, D. M., Volino, R. J., and Bejan, A. Conditionally-sampled turbulent and non-turbulent measurements of entropy generation rate in the transition region of boundary layers. *J. Fluids Eng. 129* (2007), 659–664.

[65] Wang, H. P., Goldstein, R. J., and Olson, S. J. Effect of high free-stream turbulence with large length scale on blade heat/mass transfer. *J. Turbomachinery 121* (1999), 217–224.

[66] White, F. *Viscous Fluid Flow*, third ed.

[67] Zaki, T. A., and Durbin, P. A. Mode interaction and the bypass route to transition. *J. Fluid Mech. 531* (2005), 85–111.

[68] Zaki, T. A., and Durbin, P. A. Continuous mode transition and the effects of pressure gradient. *J. Fluid Mech. 563* (2006), 357–388.

Appendix A

PTV Instantaneous Gradients

A.1 Spanwise Component of the Velocity Measurement from Continuity

The mezzo FOV images are of course 2D from the single camera set up of the PTV; therefore the need to remove certain terms in equation 2.2 was needed. All the terms involving a z- component of the flow were neglected, with the exception of the dw/dz term which was computed from continuity

$$\frac{\partial w}{\partial z} = -\frac{\partial u}{\partial x} - \frac{\partial v}{\partial y} \tag{A.1}$$

with the local Kolomogorov scale, η, never going below $3x10^{-5}$ m, and the PTV grid on the same order of magnitude it was assumed to be sufficient to calculate equation A.1. As a precaution, a convergence study was done on the central differencing scheme performed to calculated the gradients. In this case du/dy was computed with various spacings between the nodes i-1 and i+1 in the central differencing scheme. Figure A.1 shows that even at a dy of 15 grid nodes in each direction to calculate the central difference, there is no large change in value/magnitude. Therefore, a need to run PTV at a smaller grid (taking massive amounts of CPU and RAM) is not needed.

A.2 Behavior of Instantaneous Velocities in the Vicinity of the Wall

It has been shown by others in theory and with empirical data that behavior of the gradients near the wall follow the understanding of the no slip condition at the

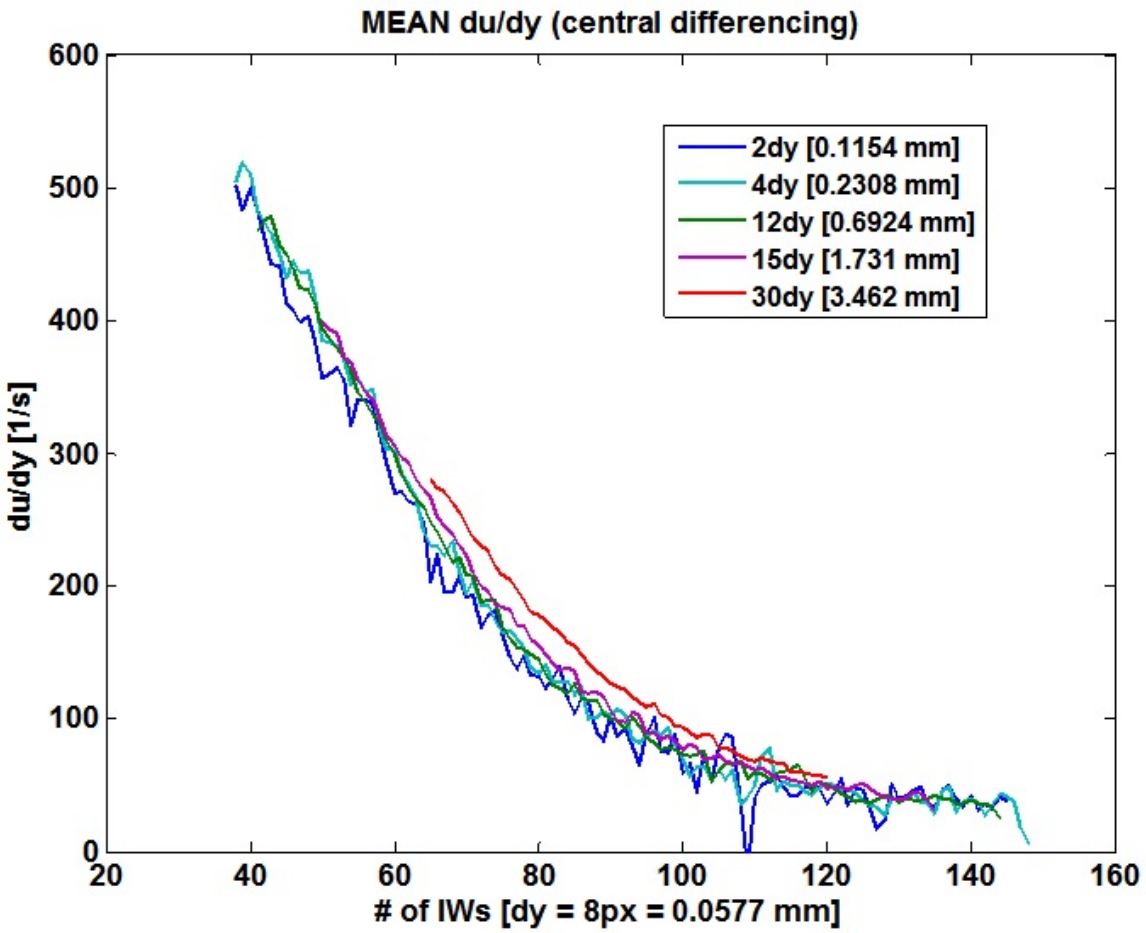

Figure A.1: Central differencing convergence study on PTV grid size.

wall. That is

$$u = v = w = 0 \text{ at } y = 0 \tag{A.2}$$

This, in turn, means that all gradients (time averaged and instantaneous) at the wall with respect to the x-, or z-directions are also zero,

$$\left.\frac{du}{dx}\right|_w = \left.\frac{du}{dz}\right|_w = \left.\frac{dv}{dx}\right|_w = \left.\frac{dv}{dz}\right|_w = \left.\frac{dw}{dx}\right|_w = \left.\frac{dw}{dz}\right|_w = 0 \tag{A.3}$$

Finally, the wall normal velocity gradient, dv/dy, is also zero at the wall, from the relationship found in continuity

$$\left.\frac{dv}{dy}\right|_w = -\left.\frac{du}{dx}\right|_w - \left.\frac{dw}{dz}\right|_w = 0 \tag{A.4}$$

which, from equation A.3, dv/dy is 0. This means that the last two gradients in the flow, du/dy and dw/dy are non-zero at the wall. This can be readily seen in Figure A.2 and A.3 where each term has been normalized by the local boundary layer thickness and freestream velocity. All gradients are trending downward at a close proximity to the wall, except for the two terms that incorporate du/dy and dw/dy (not shown). It is interesting to note that dv/dy is directly measured from the PTV, and is strongly trending towards the zero gradient at the wall – as to be expected from theory.

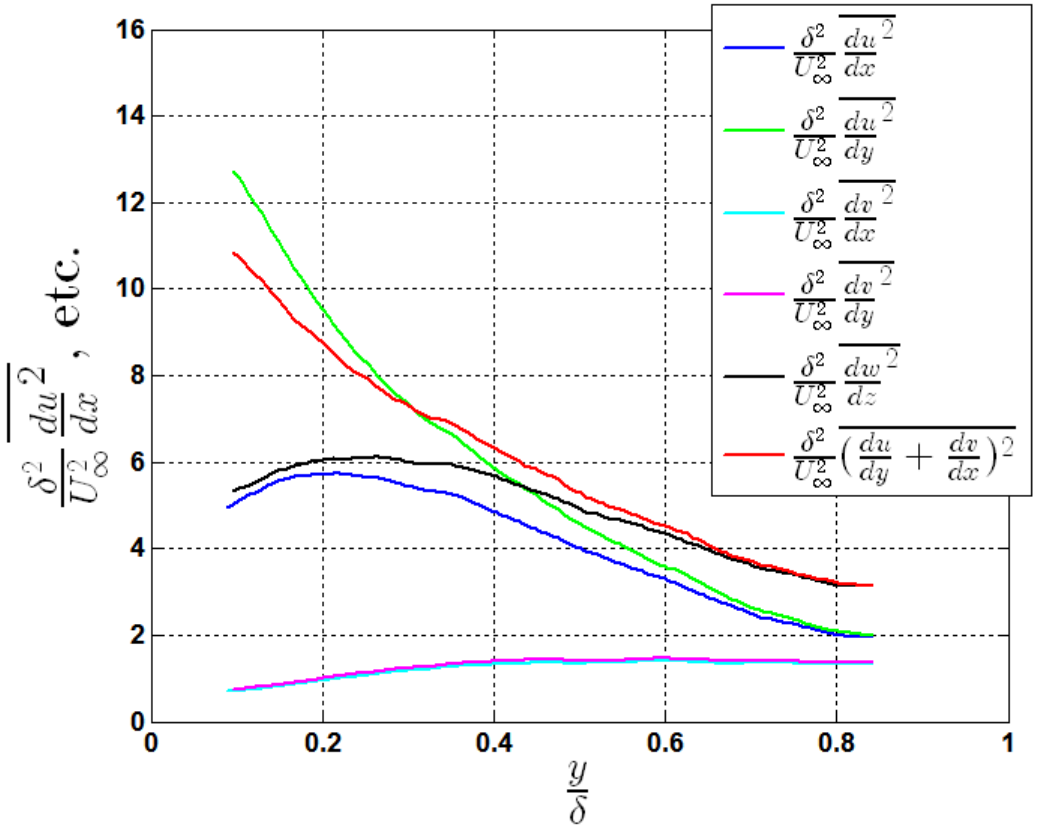

Figure A.2: Near wall instantaneous gradient behavior, at $\sqrt{Re_x} = 135$, in ZPG with TG flow condition.

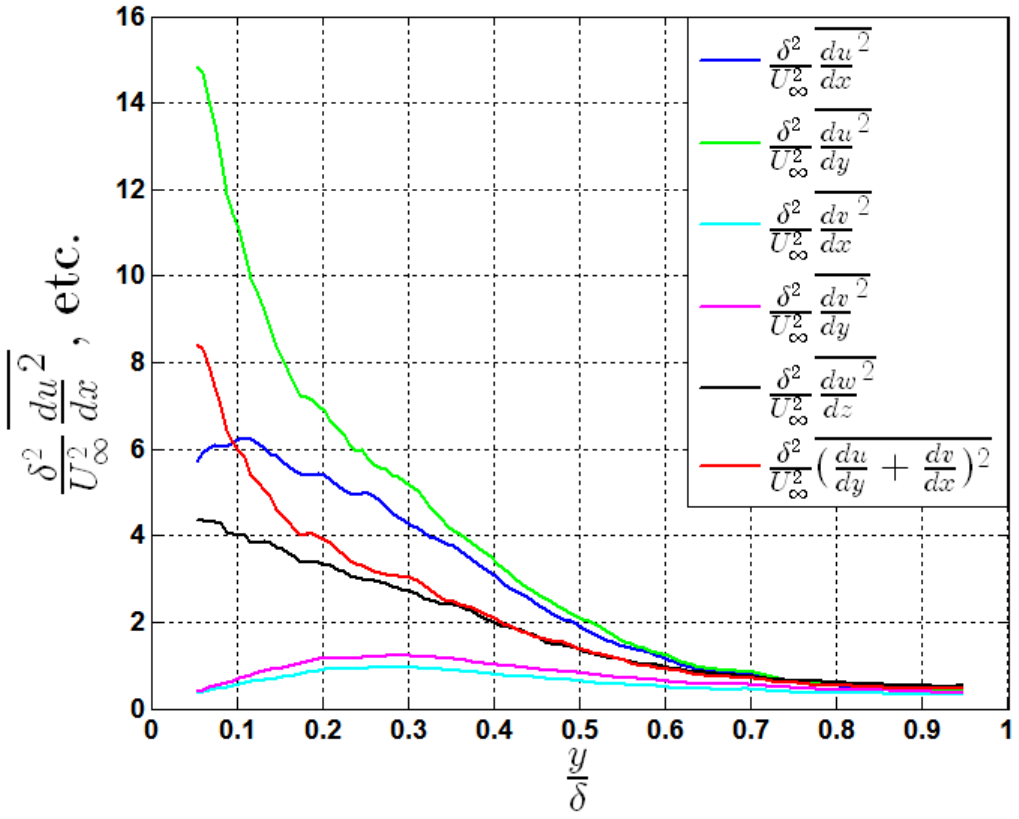

Figure A.3: Near wall instantaneous gradient behavior, at $\sqrt{Re_x} = 143$, in APG with TG flow condition.